JOURNAL OF COMPUTATIONAL PHYSICS **144,** 626–661 (1998)
ARTICLE NO. CP985925

Vlasov Simulations Using Velocity-Scaled Hermite Representations

Joseph W. Schumer*,[1] and James Paul Holloway†

*Code 6770, Naval Research Laboratory, Washington, DC 20375; †2943 Cooley Building, Nuclear Engineering and Radiological Sciences, 2355 Bonisteel Boulevard, University of Michigan, Ann Arbor, Michigan 48109-2104
E-mail: schumer@calvin.nrl.navy.mil and hagar@engin.umich.edu

Received August 28, 1997; revised January 13, 1998

The efficiency, accuracy, and stability of two different pseudo-spectral methods using scaled Hermite basis and weight functions, applied to the nonlinear Vlasov–Poisson equations in one dimension (1d-1v), are explored and compared. A variable velocity scale U is introduced into the Hermite basis and is shown to yield orders of magnitude reduction in errors, as compared to linear kinetic theory, with no increase in workload. A set of Fourier–Hermite coefficients, representing a periodic Gaussian distribution function, are advanced through time with an $O(\Delta t^2)$-accurate splitting method. Within this splitting scheme, the advection and acceleration terms of the Vlasov equation are solved separately using an $O(\Delta t^4)$-accurate Runge–Kutta method. The asymmetrically weighted (AW) Hermite basis, which has been used previously by many authors, conserves particles and momentum exactly and total energy to $O(\Delta t^3)$; however, the AW Hermite method does *not* conserve the square integral of the distribution and is, in fact, numerically unstable. The symmetrically weighted (SW) Hermite algorithm, applied here to the Vlasov system for the first time, can either conserve particles and energy (for N_u even) or momentum (for N_u odd) as $\Delta t \to 0$, where N_u is the largest Hermite mode number. The SW Hermite method conserves the square integral of the distribution and, therefore, remains numerically stable. In addition, careful velocity scaling improves the conservation properties of the SW Hermite method. Damping and growth rates, oscillation frequencies, E-field saturation levels, and phase-space evolution are seen to be qualitatively correct during simulations. Relative errors with respect to linear Landau damping and linear bump-on-tail instability are shown to be less than 1% using only 64 velocity-scaled Hermite functions. Comparisons to particle-in-cell (PIC) simulations show that as the number of particles increases to more than 10^6, the PIC solutions converge to scaled SW Hermite solutions that were found in only $1/10$ of the run-time. The SW

[1] Corresponding author.

0021-9991/98 $25.00
Copyright © 1998 by Academic Press
All rights of reproduction in any form reserved.

Hermite method with velocity scaling is well-suited to kinetic simulations of warm plasmas. © 1998 Academic Press

Key Words: Vlasov solvers; spectral methods.

INTRODUCTION

In this article, we describe an efficient numerical kinetic method for 1d-1v plasma simulations which can accurately resolve the fine-scales of phase-space distributions of charged particles. By efficiently evolving these distributions while maintaining numerical stability, preserving several physical constants-of-motion, and making reliable linear and nonlinear physical predictions, we will demonstrate this one-dimensional method as a benchmark and as a promising alternative to other accepted numerical kinetic methods for collisionless charged-particle systems.

One of the weighted residuals methods described below, the symmetrically weighted (SW) Hermite method, uses Hermite functions in velocity as both basis and weight functions and will prove to be most efficacious. A method based on Hermite basis functions but Hermite polynomial weights, the asymmetrically weighted (AW) Hermite method, will prove to be less stable, even though the AW Hermite method has better conservation properties overall. Both of these Hermite methods, when properly scaled, will prove to be superior to unscaled Hermite methods and more accurate than particle-in-cell (PIC) methods for predicting growth/damping rates and frequencies of warm plasma phenomena. In the rest of this introduction, we will describe the basic physical model being examined and some of the numerical techniques that have been used previously to treat it.

The one-dimensional (1d-1v) collisionless evolution of a charge-neutralized electron plasma is governed by the Vlasov–Poisson equations,

$$\frac{\partial f(x,u,t)}{\partial t} + u\frac{\partial f}{\partial x} + \frac{q_e}{m_e}E(x,t)\frac{\partial f}{\partial u} = 0 \tag{1}$$

$$\frac{\partial E(x,t)}{\partial x} = \frac{q_e}{\epsilon_o}\int_{-\infty}^{\infty} f(x,u,t) - f_i(u,0)\,du, \tag{2}$$

where $f(x,u,t)$ is the electron distribution function, put in terms of the independent phase-space variables, position $x \in [-L/2, L/2]$, velocity $u \in (-\infty, \infty)$, and time t. The electron charge q_e, mass m_e, and the permittivity of free-space ϵ_0 are in rationalized mks units. In the simulations shown here, we model the evolution of electron plasma waves neutralized by a free-streaming spatially uniform ion background $f_i(u,0) = \int f(x,u,0)\,dx$; hence, the spatially averaged electric field is zero for all time. This standard model [1, 2] of an electron plasma with infinitely massive ions is consistent with Ampere's law [3], provided that the spatially averaged initial current is zero for all time.

Kinetic methods, which include PIC and Vlasov solvers, are required for problems with complicated field-particle interactions in plasmas with evolving phase-space profiles that cannot be accurately modeled with charged fluid descriptions. PIC and cloud-in-cell (CIC) algorithms have been developed [4, others], quite frequently used, and have become standard technologies in the design and evaluation of neutral and nonneutral plasma systems. However, PIC/CIC codes, based on the modeling of plasmas using 10^2 to 10^7 macroparticles, are inherently noisy. In plasmas with tenuous velocity–space profiles there might be few "numerical" particles coinciding with the phase velocities of the electrostatic waves.

In addition, collisionless plasmas can have fine-scale phase-space structures, such as "cat's eyes [5]," that call for very precise modeling. While PIC methods are relatively easy to implement, Vlasov solvers, in contrast, are free of artificial discrete particle noise, may be better suited for warm or tenuous plasmas and can model low density regions of phase space as accurately as they model high density regions.

Besides spectral Vlasov solvers, which will be outlined further below, one may choose to use standard finite difference schemes [6], finite elements schemes [7], or methods which integrate the distribution along "characteristic orbits" [8–10]. All three require a low-order interpolation to either calculate derivatives or to map the distribution back onto a fixed grid. These schemes can produce numerical smoothing, which has a beneficial effect because it reduces the secular increase of velocity derivatives with time (a fundamental problem in *collisionless* plasma simulations [9, 11]); nevertheless, this benefit is gained by compromising physical fidelity with the introduction of artificial dissipation and incorrect dispersion. In general, conservation of particles, momentum, and energy is only approximate in such methods.

Weighted-residuals and pseudospectral methods tend to generate conservative and nondispersive schemes [12]. Hence, spectral methods are ideally suited for modeling collisionless plasmas in which the evolution of the fine-scales is significant. Many suitable sets of basis and weight functions have been used for the spectral discretization of the Vlasov–Poisson system in one or more dimensions. Because the velocity profile of solutions of the Vlasov equation naturally develop fine scales which are difficult to resolve (a process known as "filamentation" [9, 11, 13, 14]), special attention must be given to the representation of velocity space. Fourier-based velocity representations [13, 15] cannot conserve momentum due to the periodicity of the basis; particles with large positive velocities may be accelerated and instantly become particles with large negative velocities. Errors in particle momentum, by coupling between electrostatic waves and particles with velocities near the phase velocity of the wave, can lead to errors in electrostatic wave damping and growth. The Chebyshev velocity representation in [16] also does not conserve momentum or total energy.

The normalized Hermite basis is a natural choice for Maxwellian-like velocity profiles because the lowest order expansion function is a Gaussian function [17]. One of the main objectives of this article is to demonstrate the benefits and limitations of two different biorthonormal sets of Hermite basis and weight functions, namely, asymmetrically weighted (AW) and symmetrically weighted (SW) Hermite bases, given by

$$\text{SW: } \Psi_n(v) = \Psi^n(v) = C_n e^{-v^2/2} H_n(v) \tag{3}$$

$$\text{AW: } \Psi_n(v) = C_n e^{-v^2} H_n(v), \quad \Psi^n(v) = C_n H_n(v), \tag{4}$$

where $H_n(v)$ is the standard Hermite polynomial normalized so that $H_n(v) \sim 2^n v^n$ for large v and $C_n = (\pi^{1/4}\sqrt{2^n n!})^{-1}$. In the weighted residuals methods to be developed here, superscripted functions are weight functions and subscripted functions are basis functions. Detailed analysis will later show that algorithms derived from these two bases yield different conservation properties, optimization characteristics, and numerical stability criteria.

No Vlasov method based on the SW Hermite representation has been developed until this time. Fourier–Hermite (FH) weighted-residual schemes [14, 18–20] in (x, u) using AW Hermite functions have been implemented before but were dismissed because of their poor velocity resolution properties [21]. However, recent work suggests that with proper

selection of the system velocity scale length, the Hermite basis can be quite competitive when modeling functions with Gaussian-shaped profiles [22–24] such as thermally warm plasmas. Without careful velocity-scaling of the Hermite functions, however, fine-scales develop at the level of the coarse velocity grid, requiring spectral expansions ranging from 500 to 1500 Hermite modes to achieve only moderate accuracy levels [21, 25, 26]. To alleviate this requirement, some of these earlier FH algorithms incorporated artificial damping or monotonic reduction of the Hermite expansion order N_u over time [14, 25–27]; unfortunately, artificial damping changes the interesting collisionless physics and decreasing N_u eventually leaves the simulation with no velocity resolution whatsoever.

In addition, previous Vlasov algorithms designed around FH weighted-residual methods were unnecessarily inefficient. By evaluating the nonlinear term $E\,\partial_u f$ of Eq. (1) in transformed Fourier space, an additional $O(N_x)$ operations per coefficient per time-step were incurred, where N_x is the number of spatial mode numbers. In this article, we employ an $O(\Delta t^2)$-accurate splitting technique similar to that used by Cheng and Knorr [9] and Klimas and Farrell [13] which decouples the advection (free-streaming) and acceleration terms of the Vlasov equation (1) into two separate first-order partial differential equations. Separating the two-terms of Eq. (1) and performing the nonlinear multiply $E\,\partial_u f$ in x-space makes the algorithm more efficient (a more detailed operational count is shown below) with an acceptable level of accuracy due to the small Δt used in the study of "collisionless" phenomena.

For the simulations presented here the spatial dependence of the plasma distribution function $f(x, u, t)$ is assumed to be periodic and is, therefore, represented with a Fourier basis in space. The velocity profile is, at least initially, assumed to be Maxwellian-like and is represented with one of the two different bi-orthonormal Hermite basis sets (SW and AW) described above. These basis sets are used to develop a weighted-residual advection equation and a collocation acceleration equation (in x-space) for application of the splitting scheme.

To optimize the Hermite representations, we introduce a velocity-scale U to be used during simulations as a parameter to enhance spectral accuracy [22]. One goal of this article is to compare the velocity-scaled AW and SW Hermite methods against unscaled representations. We will show that for a fixed number of unknowns using the optimal U-scale can improve conservation properties and solutions considerably, thereby allowing a reduction in the needed number of unknowns for a desired precision level and making the method more efficient. Another goal is to point out that the SW Hermite method is superior to the AW Hermite method because it conserves $\int\int f^2\,dx\,du$ while the latter does not, thereby assuring long-time stability of the SW Hermite method.

Analysis and comparison of the SW and AW Hermite algorithms will focus on efficiency, numerical stability, scaling of errors with velocity expansion order N_u and velocity-scale U, and conservation of important physical quantities, such as particles, momentum, and total energy in the fully discrete system. In addition, a periodic PIC code ES1 [4] will be used as a reference to test the two FH methods, basing the comparison on their respective modeling of the Landau damping phenomena in a nearly uniform Maxwellian plasma and their modeling of electrostatic instabilities in a plasma with a "bump-on-tail" profile.

THE SPLITTING ALGORITHM

To improve the computational efficiency of the FH spectral method to be developed below, we employ a well-known splitting technique used by Cheng and Knorr [9] and Klimas and Farrell [13] which decouples the advection and acceleration terms in the Vlasov equation

using separate mappings $\mathbf{X}$ and $\mathbf{V}$,

$$f(x,u,t_o+\Delta t)=\mathbf{X}_{\Delta t/2}\mathbf{V}_{\Delta t}\mathbf{X}_{\Delta t/2}\ f(x,u,t_o)+O(\Delta t^3). \tag{5}$$

Here the advection mapping $\mathbf{X}$ is the solution of $\dot{\mathbf{X}}=-u\partial_x\mathbf{X}$ with $\mathbf{X}(0)=\mathbf{I}$; this map free-streams the distribution $f(x,u,t)$ in space at a constant velocity for time $\Delta t/2$. The acceleration mapping $\mathbf{V}$ is the solution of $\dot{\mathbf{V}}=-(q_e/m_e)\,E(x)\partial_u\mathbf{V}$ with $\mathbf{V}(0)=\mathbf{I}$; this map accelerates the distribution $f(x,u,t)$ in velocity with a constant acceleration $q_eE(x)/m_e$ forward in time Δt. We shall see later that this method is more efficient than a similar unsplit algorithm.

Rather than explicitly mapping the distribution function using Eq. (5), we advance $f(x,u,t)$ forward one time step by numerically solving, in order, the following sequence of differential equations, each taking its initial data from the previous step:

$$\mathbf{X}_{\Delta t/2}\Leftrightarrow \frac{\partial f(x,u,t)}{\partial t}=-u\frac{\partial f}{\partial x},\ f(x,u,t_o) \quad\rightarrow\ f(x,u,t_a) \tag{6}$$

$$\text{Poisson}\qquad \frac{\partial E(x,t_a)}{\partial x}=\frac{q_e}{\epsilon_o}\left[\int_{-\infty}^{\infty}f(x,u,t_a)\,du-n_o\right]\rightarrow E(x,t_a) \tag{7}$$

$$\mathbf{V}_{\Delta t}\Leftrightarrow \frac{\partial f(x,u,t)}{\partial t}=-\frac{q_e}{m_e}E(x,t_a)\frac{\partial f}{\partial u},\ f(x,u,t_a) \quad\rightarrow\ f(x,u,t_b) \tag{8}$$

$$\mathbf{X}_{\Delta t/2}\Leftrightarrow \frac{\partial f(x,u,t)}{\partial t}=-u\frac{\partial f}{\partial x},\ f(x,u,t_b) \quad\rightarrow\ f(x,u,t_o+\Delta t). \tag{9}$$

The effective algorithmic sequence is shown schematically in Fig. 1 in a phase space of spatial length L with maximum resolved velocity u_{max}. The temporal positions $t_a=t_o+\Delta t/2$ and $t_b=t_a+\Delta t$ are not physically realizable points in time but are only used for labeling the algorithmic steps. Solution of Eq. (6) free-streams $f(x,u,t_o)$ for a half time-step $\Delta t/2$ from time t_o to "time" t_a. After free-streaming, we calculate the E-field using $f(x,u,t_a)$ by solving Eq. (7). The distribution $f(x,u,t_a)$ is then accelerated for a full time-step Δt from "time" t_a to "time" t_b by solving Eq. (8) with $E(x,t_a)$ fixed in time. To finish the algorithm sequence, we solve Eq. (9) using the distribution information at "time" t_b by advecting $f(x,u,t_b)$ forward $\Delta t/2$ from t_b to time $t_o+\Delta t$. This splitting technique, as written, is $O(\Delta t^2)$ accurate (see Appendix A).

In practice, we may reduce the computational effort by using $\mathbf{X}_{\Delta t/2}\mathbf{X}_{\Delta t/2}\equiv\mathbf{X}_{\Delta t}$ and still retain $O(\Delta t^2)$ accuracy, provided that the half time-step advection solves $\mathbf{X}_{\Delta t/2}$ are applied at the beginning and the end of the simulation.

FOURIER–HERMITE SPECTRAL REPRESENTATION

In order to numerically solve Eqs. (6)–(9) and advance the distribution function in time, we first discretize space and velocity using Fourier–Hermite based spectral methods. The Fourier eigenfunctions $\Phi_k(x)=[\Phi^k(x)]^*=e^{ikx(2\pi/L)}$, orthogonal in the domain $[-L/2\le x\le L/2]$, are ideally suited for representing the assumed spatially periodic distribution function. For the velocity dependence of the distributions $f(x,u,t)$, we choose basis functions which have a Gaussian as their zeroth-order basis function, the orthonormal Hermite functions. In this article, we will compare algorithms derived from the two basis sets of bi-orthonormal Hermite polynomials introduced previously in Eqs. (3) and (4),

$$\text{SW: }\Psi_n(v)=\Psi^n(v)=C_ne^{-v^2/2}H_n(v) \tag{10}$$

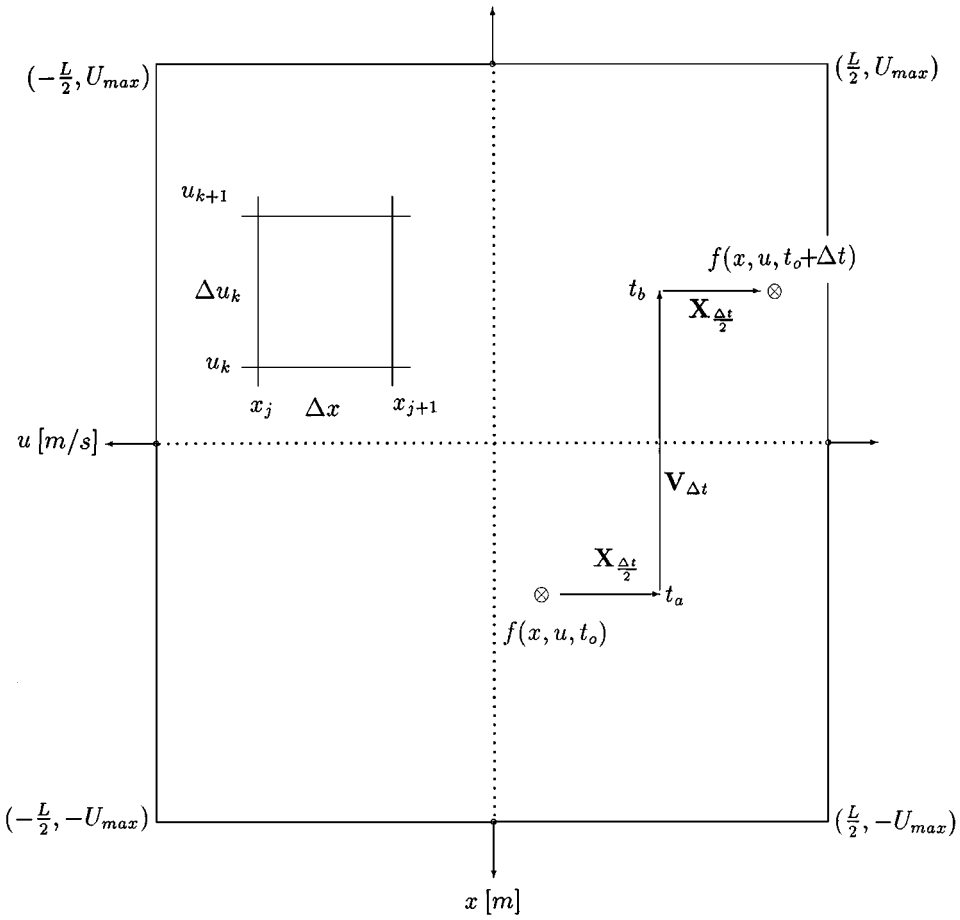

FIG. 1. One-dimensional phase space grid and effective particle motion in the splitting scheme. The spatial resolution is uniform while the velocity resolution is nonuniform, defined by the Gauss quadrature points.

$$\text{AW: } \Psi_n(v) = C_n e^{-v^2} H_n(v), \quad \Psi^n(v) = C_n H_n(v), \tag{11}$$

where $H_n(v)$ is the nth Hermite polynomial normalized so that $H_n(v) \sim 2^n v^n$ as $v \to \infty$ [17], $C_n = (\pi^{1/4}\sqrt{2^n n!})^{-1}$ is a normalization constant, and $v = u/U$ is a dimensionless velocity, scaled by the optimizing velocity scale U. The use of the velocity scale U can greatly improve the spectral accuracy of Hermite-based representations of Gaussian-shaped functions [22–24]. However, the practical benefits of velocity scaling have not been previously applied to modeling of the nonlinear Vlasov–Poisson system.

Both Hermite bases are bi-orthonormal in the infinite domain, meaning that

$$\int_{-\infty}^{\infty} \Psi^m(v)\Psi_n(v)\, dv = \delta_n^m, \tag{12}$$

and they satisfy two-term recursion relations [17],

$$\begin{bmatrix} v\Psi^n(v) \\ v\Psi_n(v) \end{bmatrix} = \sqrt{\frac{n+1}{2}} \begin{bmatrix} \Psi^{n+1}(v) \\ \Psi_{n+1}(v) \end{bmatrix} + \sqrt{\frac{n}{2}} \begin{bmatrix} \Psi^{n-1}(v) \\ \Psi_{n-1}(v) \end{bmatrix}, \tag{13}$$

and derivative relations,

$$\text{SW: } \frac{d}{dv}\begin{bmatrix}\Psi^n(v)\\ \Psi_n(v)\end{bmatrix} = -\sqrt{\frac{n+1}{2}}\begin{bmatrix}\Psi^{n+1}(v)\\ \Psi_{n+1}(v)\end{bmatrix} + \sqrt{\frac{n}{2}}\begin{bmatrix}\Psi^{n-1}(v)\\ \Psi_{n-1}(v)\end{bmatrix} \tag{14}$$

$$\text{AW: } \frac{d}{dv}\begin{bmatrix}\Psi^n(v)\\ \Psi_n(v)\end{bmatrix} = \begin{bmatrix}\sqrt{2n}\Psi^{n-1}(v)\\ -\sqrt{2(n+1)}\Psi_{n+1}(v)\end{bmatrix} \tag{15}$$

for $n \geq 0$.

The Fourier–Hermite representation for the plasma distribution function $f(x,u,t)$ is written, using either the AW or SW basis, as

$$f(x,u,t) = \sum_{m=-N_x/2}^{N_x/2-1}\sum_{n=0}^{N_u} f^{mn}(t)\Phi_m(x)\Psi_n(v), \tag{16}$$

where $v = u/U$, m is the Fourier mode number, n is the Hermite mode number, and the functions $\Phi_m(x)$ and $\Psi_n(v)$ are the Fourier and Hermite basis functions, respectively. In our method, the initial coefficients $f^{mn}(0)$ are calculated by numerical integration of the initial distribution function $f(x,u,0)$ with the Fourier and Hermite weight functions $\Phi^m(x)$ and $\Psi^n(v)$. Using Gauss quadrature formulas suitable for Fourier and Hermite bases, we may write

$$f^{mn}(0) = \frac{1}{U}\iint f(x,u,0)\Phi_m(x)\Psi_n(v)\,dx\,du \tag{17}$$

$$\approx \frac{1}{N_x U}\sum_{j=0}^{N_x}\Phi_m(x_j)\sum_{k=0}^{N_u} w_k\Psi_n(v_k)\,f(x_j,u_k,0). \tag{18}$$

The coefficients $f^{mn}(0)$ are used as initial conditions for the FH simulations to be presented. The N_x spatial points x_j are equispaced between $[-L/2, L/2]$, including one endpoint. In practice, the sum over the index j is performed using a standard fast Fourier transform (FFT) routine. The N_u+1 Gauss–Hermite quadrature points u_k are determined by the roots $\Psi_{N_u+1}(v_k)=0$ and scaling $u_k = U v_k$. The Gauss–Hermite quadrature weights w_k used in Eq. (18) are given [17] by

$$w_k = \frac{2^{N_u}(N_u!)\sqrt{\pi}}{(N_u+1)\left[H_{N_u}(v_k)\right]^2} \times \begin{cases} e^{v_k^2}, & \text{AW},\\ e^{v_k^2/2}, & \text{SW}.\end{cases} \tag{19}$$

With the Hermite scale U, the maximum resolved velocity in the system is $u_{max} = v_{N_u}U$, noting that $v_{N_u} \sim \sqrt{N_u}$. Interior roots of the Hermite polynomials are *not* equispaced in $[-u_{max}, u_{max}]$ but have the highest velocity resolution in the center of the system near $u=0$; i.e., fine-scale structures near $u=0$ are more highly resolved with Hermite-based methods. After initially calculating the Fourier–Hermite coefficients $f^{mn}(0)$, no further Hermite transforms are required until the output is postprocessed for display, thereby avoiding $O(N_u)$ operations per coefficient per time-step.

For spectral accuracy of the SW Hermite representation (i.e., $|f^n| < Cn^{-p}\ \forall p$ and some constant $C>0$), the results in [22] require that the distribution be infinitely differentiable

and exponentially decaying as $|u| \to \infty$, e.g. $f(u) = e^{-|u|}$. Because of the Hermite normalizations, these conditions imply that the AW Hermite representation is limited to larger values of velocity scale U in order to satisfy the bound

$$|f(u)| < M \exp\left(-\rho \frac{u^2}{2U^2}\right) \tag{20}$$

for constants $M > 0$ and $\rho > 1$. For example, when expanding a Maxwellian distribution of thermal width v_{th} using the AW Hermite basis, the velocity scale U must satisfy $U > U_{min} = v_{th}/\sqrt{2}$. The restriction thus implied for the AW Hermite expansion is slightly cumbersome. Because the maximum resolved velocity u_{max} is proportional to U, the AW Hermite expansions will have minimum allowable resolution $\Delta u \sim v_{th}/\sqrt{N_u}$. The SW Hermite expansions are not so limited. One of our goals is to assess the benefits and limitations of each Hermite method over a wide range of velocity scales U, especially with these scaling limits in mind.

To develop equations for the advection mapping $\mathbf{X}_{\Delta t/2}$, we multiply Eq. (6) by $\Phi^m(x)\Psi^n(v)$ and integrate to find a system of ordinary differential equations (ODEs) for the advection of the distribution $f(x, u, t)$, cast in terms of the FH coefficients $f^{mn}(t)$. These ODEs are written

$$\frac{\partial f^{mn}(t)}{\partial t} = -\frac{i\sqrt{2}\pi m U}{L}[\sqrt{n+1}\, f^{m,n+1}(t) + \sqrt{n}\, f^{m,n-1}(t)], \tag{21}$$

where we used $v = u/U$ in the Hermite weight functions. Equation (21) was derived using the two-term Hermite recursion relation shown in Eq. (13), so the AW and SW formulas have the same form. The solution of this system of $N_x(N_u + 1)$ coupled ODEs is called the "X-shift." In this work, these ODEs are solved using an $O(\Delta t^4)$-accurate Runge–Kutta (RK4) algorithm [28] to advance the distribution $f(x, u, t)$ forward $\Delta t/2$ from time t_o to "time" t_a and again from "time" t_b to time $t_o + \Delta t$ (see Fig. 1).

A time-stepping scheme with a rather large absolute stability region such as RK4 can be very useful for kinetic problems. The use of a high-order RK scheme reduces the influence of the very few fast moving particles which set the Courant limit. An RK2 scheme is unstable for imaginary (oscillatory) eigenvalues and so it is unsuitable for a collisionless kinetic problem, while use of an RK3 scheme would require an increase in the number of operations because of its smaller stability regime. To obtain adequate stability with the $O(\Delta t^3)$-accurate Adams–Bashforth (AB3) scheme, the computational workload increases up to 2.5 times, compared to the RK4 method for the present application. These computational efficiency comparisons will be discussed in detail below. In these simulations, the RK4-based splitting scheme was chosen on the basis of high efficiency and stability. Other more accurate time-stepping schemes could probably be designed as well.

It is important to note the truncation error introduced by the X-shift through the $n = N_u$ equations for all of the nonzero Fourier modes m. To close the set of coupled ODEs, we arbitrarily set the coefficients $f^{m,N_u+1}(t)$ to zero (other closure schemes have been discussed; for example, see Refs. [14, 26]). In the exact system with an infinite number of Hermite coefficients, the coefficients $f^{m,N_u+1}(t)$ are, of course, *not* zero. Fortunately, this truncation error can be made small if we have a spectrally accurate representation for $f(x, u, t)$; for functions with singularities in the complex-v plane the error in the SW Hermite expansion is

$$f^{m,N_u+1} \sim O\left(N_u^{-1/4} e^{-w(2N_u+1)^{1/2}}\right), \tag{22}$$

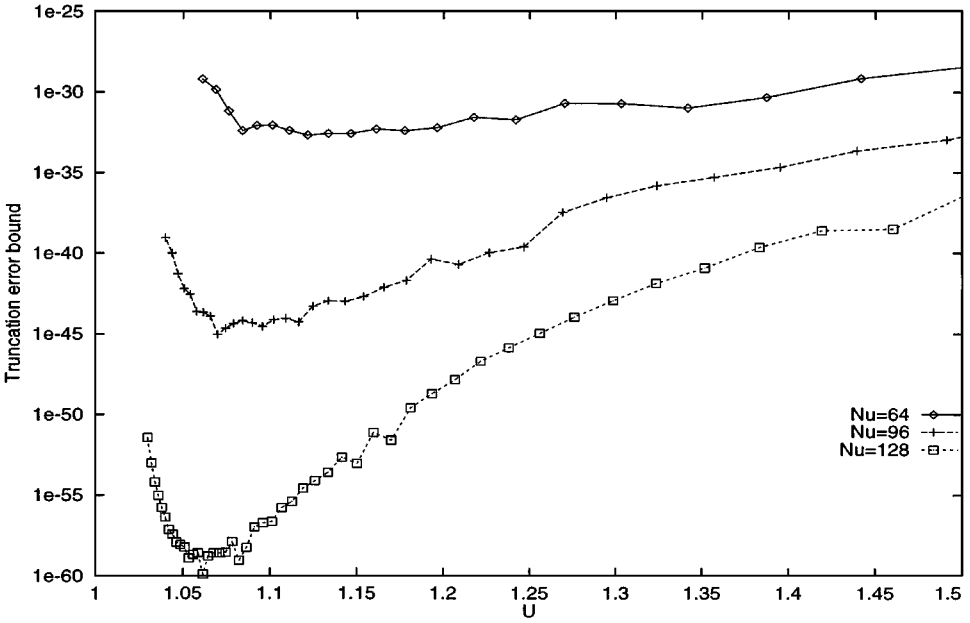

FIG. 2. Truncation error estimates versus the velocity scale U using the AW Hermite method for a "bump-on-tail" distribution. Thermal velocity and drift velocity were arbitrarily fixed at $v_{th} = 1.32619$ m/s and $v_d = 5$ m/s, respectively.

where w is the distance from the real axis to the nearest singularity [22]. Reducing the velocity scale U can improve spectral accuracy by increasing w and reduce the truncation error by orders of magnitude. However, the estimate in Eq. (22) is valid only for asymptotically large N_u; since the maximum resolved velocity $u_{max} \propto U\sqrt{N_u}$, making U too small may require a larger N_u in order to well-represent the tails of the Maxwellian. On the other hand, if U is too large, the distribution appears narrow and requires high-order Hermite functions to represent the large gradients. We therefore expect an optimal *intermediate* value of U and that finding this optimal value will result in dramatic decreases in the truncation error. Figure 2 shows the change in the ratio $|f^{N+1}/f^0|$ versus velocity-scale U from the AW Hermite expansion of the bump-on-tail distribution in Fig. 15; we see that selection of the optimal scale length U for a fixed value of N_u results in orders of magnitude reduction in the truncation error.

In order to avoid the numerically expensive convolution sum resulting from the nonlinear term $E\partial_u f$, the acceleration mapping $\mathbf{V}_{\Delta t}$ is applied by solving a differential equation for the Hermite coefficients $f^n(x,t)$ in x-space. Multiplying Eq. (8) by the Hermite weighting function $\Psi^n(v)$ and integrating, we find a system of ODEs for the Hermite coefficients $f^n(x,t)$, written

$$\frac{\partial f^n(x,t)}{\partial t} = \frac{\sqrt{2}q_e E(x,t_a)}{m_e U} \begin{cases} \sqrt{n}\, f^{n-1}(x,t), & \text{AW}, \\ -\frac{1}{2}[\sqrt{n+1}\, f^{n+1}(x,t) - \sqrt{n}\, f^{n-1}(x,t)], & \text{SW}, \end{cases} \tag{23}$$

where $v = u/U$. Both of these systems of equations in Eq. (23) were derived after integration by parts and use of the Hermite derivative relations in Eqs. (14) and (15).

Solution of either set of coupled equations in Eq. (23) is called a "V-shift." The V-shift is performed using an RK4 method for each Hermite coefficient on the x-grid and effectively accelerates the distribution $f(x,u,t_a)$ at "time" t_a forward one time-step Δt to "time"

t_b. Because the X-shift is performed using coefficients $f^{mn}(t)$, a Fourier transform must be performed before (to get $f^n(x, t_a)$) and after (to get $f^{mn}(t_b)$) each V-shift. The E-field $E(x, t_a)$, calculated by solving Poisson's equation (described below), is held *constant* during the V-shift. Hermite transforms costing $O(2N_u)$ operations per coefficient are not required during the simulations; only the initial Hermite coefficients $f^n(x, 0)$ are needed.

The AW Hermite V-shift equations shown in Eq. (23) form a closed system; because $f^{N_u+1}(x, t)$ is not required, the truncation error comes only from the AW Hermite X-shift equations. In contrast, the SW Hermite X-shift and V-shift have very similar formulas, both requiring some truncation condition for which we use $f^{m,N_u+1} = 0$. As stated earlier, the velocity space truncation errors in each method may be reduced with a well-chosen velocity scaling or by increasing the Hermite order N_u.

Exact advection and acceleration mappings for the AW Hermite algorithm have been derived [29], but the computational cost is $O(N_u)$ operations per coefficient, as compared to $O(1)$ per coefficient for the RK4 scheme. Exact X-shifts and V-shifts would allow no gains in accuracy due to the $O(\Delta t^3)$ errors of the splitting method. It is interesting to note, however, that *exact* solutions of the field-free problem (pure free streaming) and the spatially uniform problem (plasma oscillations) can be recovered [24] using the AW Hermite method.

Before we can apply the V-shift, we need to evaluate the electric field $E(x, t_a)$ at time t_a (see Fig. 1). Inserting Eq. (16) into Poisson's equation (7) and using the Hermite basis functions, we find

$$\frac{\partial E(x, t_a)}{\partial x} = \frac{q_e U}{\epsilon_o} \sum_{m=-N_x/2}^{N_x/2-1} g^{m0}(t_a) \Phi_m(x), \tag{24}$$

where

$$g^{m0} = \begin{cases} f^{m0}(t_a), & \text{AW}, \\ \sum_{n=0}^{N_u} I_{0n} f^{mn}(t_a), & \text{SW}. \end{cases} \tag{25}$$

The coefficients I_{0n} are given by the recursion

$$I_{0n} = \int_{-\infty}^{\infty} \Psi_n(\lambda)\, d\lambda = \sqrt{\frac{n-1}{n}} I_{0,n-2} \tag{26}$$

with $I_{00} = \sqrt{2}\pi^{1/4}$ and $I_{01} = 0$. With the E-field Fourier representation, $E(x, t_a) = \sum_m E^m(t_a)\Phi_m(x)$, we may perform differentiation with respect to x,

$$\frac{\partial E(x, t_a)}{\partial x} = \sum_{m=-N_x/2}^{N_x/2-1} \left(\frac{2\pi i m}{L} E^m(t_a) \right) \Phi_m(x), \tag{27}$$

and then identify the coefficients $E^m(t_a)$ in Eqs. (24) and (25), written

$$E^m(t_a) = \left(\frac{-iLq_eU}{2\pi\epsilon_o} \right) \begin{cases} \frac{1}{m} f^{m0}(t_a), & \text{AW},\ m \neq 0, \\ \frac{1}{m} \sum_{n=0}^{N_u} I_{0n} f^{mn}(t_a), & \text{SW},\ m \neq 0, \\ 0, & \text{both},\ m = 0. \end{cases} \tag{28}$$

$E^0(t_a)$ is set to zero [3] for all time during the simulations shown here. The coefficients $E^m(t_a)$ in Eq. (28) are inverse Fourier transformed to $E(x_i, t_a)$ for use in the accelerating V-shift shown in Eq. (23). If an external, uniform, time-varying E-field is desired, $E^0(t_a)$ may be varied appropriately before each V-shift.

OPERATIONAL COSTS

To help assess the two methods being described here, we now provide some accounting of the floating point operations required of each. Memory access speeds may play a significant role in the design of array sizes and algorithms but will not be considered here since they are very architecture dependent. In this analysis, we will compare the fully discrete AW and SW Hermite methods, both advanced with a RK4-based $O(\Delta t^2)$-accurate splitting scheme, as formulated in the previous sections. In addition, we will compare the SW scheme to three other time-stepping options, namely (1) application of an RK3-based *split* scheme, (2) use of a Runge–Kutta based *unsplit* scheme, and (3) use of a $O(\Delta t^3)$-accurate Adams–Bashforth (AB3) *unsplit* scheme. Here, we assume the computational time required for each floating point "multiply" $\otimes$ and each "add" $\oplus$ is equal. The number of coefficients or unknowns required to represent the distribution $f(x, u, t)$ during any time-step is $N_x(N_u + 1)$.

From Eq. (21), we recall that the X-shift may be written

$$\dot{f}^{mn}(t) = A^{m,n+1} f^{m,n+1}(t) + A^{m,n} f^{m,n-1}(t), \tag{29}$$

where $A^{mn} = -i\sqrt{2n}\pi mU/L$. The RK4 scheme requires four right-hand side (RHS) evaluations of Eq. (29) with an overhead of 13 floating point operations, so the operational cost for each X-shift is 25 floating point operations per unknown. In contrast, an RK3-based X-shift would require only 19 floating point operations per unknown.

The AW and SW V-shifts may be written

$$\dot{f}^n(x, t) = \begin{cases} \Gamma^n(x) f^{n-1}(x, t), & \text{AW}, \\ -\frac{1}{2}[\Gamma^{n+1}(x) f^{n+1}(x, t) - \Gamma^n(x) f^{n-1}(x, t)], & \text{SW}, \end{cases} \tag{30}$$

where $\Gamma^n(x) = \sqrt{2n} q_e E(x)/m_e U$. In addition to the four RHS evaluations of Eq. (30) and the 13 operations of overhead for the RK4 evaluation, we must also perform two FFTs to transform the coefficients $f^{mn}(t)$ into $f^n(x, t)$ and back again. If N_x is a power of 2, each FFT costs $5 \log_2 N_x$ floating point operations per unknown. The operational cost for the V-shift is then

$$\text{Vshift Ops} = \begin{cases} [21 + 10 \log_2 N_x], & \text{AW}, \\ [29 + 10 \log_2 N_x], & \text{SW}, \end{cases} \tag{31}$$

per unknown. An RK3-based V-shift would require five fewer operations for the AW method and seven fewer operations for the SW method. Note that if the V-shift had been performed using a convolution sum,

$$E(x, t_a)\partial_u f(x, u, t) \Leftrightarrow \sum_{k=-N_x/2}^{N_x/2-1} E^{m-k}(t_a) f^n(u, t), \tag{32}$$

then the computational cost would be on the order of $O(N_x/\log_2 N_x)$ per unknown *higher* than by multiplying $E(x,t)\partial_u f(x,u,t)$ in x-space. For this reason, we perform the V-shift in real x-space with the Hermite coefficients $f^n(x,t)$.

The E-field calculation requires the evaluation of Eq. (28), which costs

$$\text{Ecalc Ops} = \begin{cases} [2+5\log_2 N_x]\,N_x, & \text{AW}, \\ [(N_u+1)+5\log_2 N_x]\,N_x, & \text{SW}, \end{cases} \tag{33}$$

floating point operations. This cost assessment includes the one FFT of the E-field modes $E^m(t_a)$ onto a spatial grid in the form $E(x_j,t_a)$. The sum over the even SW Hermite modes in Eq. (28) increases the cost of the SW Hermite E-field evaluation by $O(N_u)$ over the cost of the AW Hermite E-field evaluation.

Adding the operation costs for the X-shift, V-shift, and E-field calculation, the total number of floating point operations per time-step for the RK4-based splitting method are roughly

$$\text{Total Ops (split RK4)} = \begin{cases} [46+10\log_2 N_x], & \text{AW}, \\ [55+10\log_2 N_x], & \text{SW}, \end{cases} \tag{34}$$

per unknown. An RK3-based splitting scheme would have about 12 fewer operations per coefficient compared to these RK4-based schemes. However, if we compare the ratio of the Courant stability limits [30], $[\Delta t_{max}]_{RK4} = 1.63\,[\Delta t_{max}]_{RK3}$, we find that to obtain the same stability as the RK4-based scheme the "real" effort for the RK3-based splitting method is approximately

$$\text{Total Ops (split RK3)} \approx \begin{cases} [57+16\log_2 N_x], & \text{AW}, \\ [68+16\log_2 N_x], & \text{SW}, \end{cases} \tag{35}$$

per unknown. For $N_x = 64$, the operational workload for the RK3-based scheme is 44% larger than that of the RK4-based scheme. The Courant-limit dictated by a few very fast particles at the edge of phase-space demands a large stability regime not found in an RK3-based scheme.

Let us now consider the use of an unsplit scheme. For example, transforming the Vlasov equation using the SW Hermite basis would yield

$$\dot{f}^n(x,t) = \frac{U}{\sqrt{2}}\left[\sqrt{n+1}\frac{\partial f^{n+1}}{\partial x} + \sqrt{n}\frac{\partial f^{n-1}}{\partial x}\right] - \frac{q_e E(x,t)}{\sqrt{2}m_e U}[\sqrt{n+1}\,f^{n+1} - \sqrt{n}\,f^{n-1}]. \tag{36}$$

This set of equations may be advanced forward in time from t_o to $t_o + \Delta t$ using an RK4 scheme if the spatial derivatives are performed by $(2\pi i m/L)\,f^{mn}(t)$ in Fourier-transformed space at a cost of approximately $10\log_2 N_x$ operations per unknown. Using RK4, the total operational cost is estimated to be

$$\text{Total Ops (unsplit RK4)} = [49+40\log_2 N_x] \tag{37}$$

per unknown. For $N_x = 64$, the RK4-based method splitting scheme is nearly 2.5 times faster than the unsplit RK4 scheme, simply due to the number of $\partial_x f^n(x,t)$ evaluations.

TABLE 1
Computational Efficiency Estimates

Time-stepping method	Operations per coefficient	Relative Δt_{max}	Relative workload vs split RK4 (SW) with $N_x = 64$
split RK4 (AW)	$46 + 10 \log_2 N_x$	2.82	0.91
split RK4 (SW)	$55 + 10 \log_2 N_x$	2.82	1.00
split RK3 (SW)	$44 + 10 \log_2 N_x$	1.73	1.45
unsplit RK4 (SW)	$49 + 40 \log_2 N_x$	2.82	2.79
unsplit AB3 (SW)	$15 + 10 \log_2 N_x$	0.72	2.53

Note. A summary of the operational costs, time-stepping stability limits, and relative workload for each of the time-stepping methods considered here. The RK4-based splitting method, which is used here, has the lowest relative workload. In simulations, we found that the workload was about 6.7 μsec per coefficient per time-step.

Last, we should consider an explicit time-stepping method such as AB3 [30] which uses solutions from past time-steps and can avoid the repeated RHS evaluations of Eq. (36) required by the unsplit RK4-based scheme. The AB3 scheme, written in compact form, is

$$F(t_o + \Delta t) = F(t_o) + \Delta t\,[a\dot{F}(t_o) + b\dot{F}(t_o - \Delta t) + c\dot{F}(t_o - 2\Delta t)], \tag{38}$$

where $F(t) = [f^n(x, t)]$ and the constants are $(a, b, c) = \frac{1}{12}(23, -16, 5)$. The operational cost estimate for an unsplit AB3 method is approximately $[15 + 10 \log_2 N_x]$ operations per unknown and is clearly cheaper than the estimated $[55 + 10 \log_2 N_x]$ operations per unknown for the split RK4-based SW Hermite method. However, if we consider that the Courant stability limit imposed by the AB3 method is $[\Delta t_{max}]_{AB3} = 0.255\,[\Delta t_{max}]_{RK4}$, we see that we are required to take smaller time-steps to obtain comparable stability for a given simulation time. For $N_x = 64$, the estimated workload ratio between the unsplit AB3 and split RK4 methods is approximately

$$\left(\frac{15 + 10 \log_2 N_x}{55 + 10 \log_2 N_x}\right)\left(\frac{[\Delta t_{max}]_{RK4}}{[\Delta t_{max}]_{AB3}}\right)\Bigg|_{N_x = 64} = 2.56. \tag{39}$$

In this case, the unsplit AB3 method is 2.5 times slower than the split RK4 method.

All of the operational costs discussed in this section are summarized in Table 1. After considering the stability requirements, these cost estimates demonstrate that the RK4-based splitting scheme is efficient and well-suited for use with the Hermite methods described in this article. Although a higher accuracy time-stepping scheme could probably be designed, we have traded for efficiency and stability by choosing the RK4-based splitting scheme.

PHYSICAL CONSERVATION PROPERTIES

A numerical algorithm should, at least, approximate known conservation laws for the physical system that is being modeled. For collisionless plasmas, this is an especially interesting challenge because such plasmas possess an infinite number of conserved quantities [31]. Although a discrete model for a physical system could never capture all of these conservation laws, we would hope that a numerical kinetic method could inherently conserve important measurable quantities such as particle number, momentum, and total energy. In

TABLE 2
Conservation Properties

Fourier-Hermite method	Particles	Momentum	Energy
AW	exact	$O(\Delta t^5)$	$O(\Delta t^3)$
SW, even	$O(\Delta t^5)$	$O(\Delta t)$	$O(\Delta t^3)$
SW, odd	$O(\Delta t)$	$O(\Delta t^2)$	$O(\Delta t)$

Note. A summary of the fully-discrete conservation properties versus time-step Δt for the two Fourier-Hermite methods. Note the dependence on Hermite expansion order (even or odd) for the SW Hermite representation. The $O(\Delta t^5)$ errors come strictly from the RK4 method.

the limit of continuous time ($\Delta t \to 0$), the AW Hermite method conserves particles, momentum, and total energy; in contrast, the SW Hermite method [24] conserves both particles and energy for N_u even, yet it conserves only momentum for N_u odd. The purpose of this section is to determine whether or not the established conservation properties of these two Hermite methods survive temporal discretization under the RK4-based splitting scheme. For convenience, the conservation versus Δt scaling results derived in this section are summarized in Table 2 and the maximum conservation errors measured during simulations (to be shown later) are tabulated in Tables 3 and 4.

Particles

The total number of particles in the system is given by the integral of $f(x, u, t)$ over all phase space. For the Fourier–Hermite methods this can be written

$$\mathrm{n} = \iint f(x, u, t)\, dx\, du \tag{40}$$

$$= LU \sum_{n=0}^{N_u} f^{0n}(t) \int_{-\infty}^{\infty} \Psi_n(v)\, dv, \tag{41}$$

where we used $\Phi^0(x) = 1$, $v = u/U$, and the orthonormality relation for the Fourier basis. For the AW Hermite method, $\int_{-\infty}^{\infty} \Psi_n(v)\, dv = \delta_n^0$ because $\Psi^0(v) = 1$ and Eq. (41) becomes

$$\mathrm{n}(t) = LU f^{00}(t). \tag{42}$$

The coefficient $f^{00}(t)$ is not affected by the X-shift or the V-shift, so *particles are conserved* using the AW Hermite method, even under temporal discretization.

However, with the SW Hermite weight functions, Eq. (41) becomes

$$\mathrm{n}(t) = LU \sum_{\substack{n=0 \\ \text{even}}}^{N_u} I_{0n} f^{0n}(t), \tag{43}$$

where the coefficients I_{0n} are given recursively in Eq. (26). The X-shift does not affect $m = 0$ Fourier modes, so particles are conserved during that step.

The change in particle number during the V-shift may be written as

$$\Delta \mathrm{n} = \int [\mathrm{n}(x, t_b) - \mathrm{n}(x, t_a)]\, dx = U \sum_{\substack{n=0 \\ \text{even}}}^{N_u} I_{0n} \int \left[f^n(x, t_b) - f^n(x, t_a) \right] dx. \tag{44}$$

TABLE 3
Conservation during Landau Damping Simulations

Conserved quantity	SW (even)	SW (odd)	AW
Particles	6×10^{-15}	2×10^{-7}	1.4×10^{-16}
Momentum	6×10^{-19}	2.5×10^{-18}	1.5×10^{-18}
Total energy	1×10^{-11}	8×10^{-6}	1×10^{-11}
$J = \iint f^2 dx\, du$	1×10^{-14}	3×10^{-14}	1×10^{12}

Note. Maximum conservation errors (relative) during Landau damping simulations for the distribution and discretization listed in Table 5.

Taylor-expanding $f^n(x, t_b)$ in Δt using the V-shift equation (23) for the time-derivatives, we find that

$$\Delta \mathrm{n} = I_{0,N_u-1}\left[-\Delta t\sqrt{\frac{N_u}{2}}\frac{q_e}{m_e}\int E(x,t_a)\, f^{N_u}(x,t_a)\, dx + O(\Delta t^2)\right] + \underbrace{O(\Delta t^5)}_{RK4\ error}. \quad (45)$$

Excluding the $O(\Delta t^5)$ RK4 error, Δn is proportional to I_{0,N_u-1}. If N_u is odd then $I_{0,N_u-1} \neq 0$ and $\Delta \mathrm{n} \sim O(\Delta t)$; the magnitude of Δn, however, which is proportional to f^{N_u}, can be made exponentially small by increasing N_u or by varying U appropriately. If N_u is even, on the other hand, then *particles are conserved to* $O(\Delta t^5)$ since only the RK4 error term survives; therefore for N_u even, particle conservation errors are determined by the accuracy of the time-stepping scheme used for the V-shift.

In Tables 3 and 4, we show that the AW and SW (even) Hermite methods conserve particles nearly at round-off level ($\sim 10^{-15}$ errors), whereas the SW (odd) Hermite method has particle conservation errors ranging from 10^{-7} to 10^{-4}.

Momentum

The total momentum of the system may be written

$$p(t) = m_e \iint u f(x,u,t)\, dx\, du \quad (46)$$

$$= m_e L U^2 \sum_n f^{0n}(t) \int_{-\infty}^{\infty} v \Psi_n(v)\, dv \quad (47)$$

TABLE 4
Conservation during Bump-on-Tail Simulations

Conserved quantity	SW (even)	SW (odd)	AW
Particles	4×10^{-15}	4.5×10^{-4}	2.2×10^{-16}
Momentum	5.8×10^{-2}	9.2×10^{-5}	4×10^{-14}
Total energy	2.7×10^{-6}	1.5×10^{-2}	7×10^{-2}
$J = \iint f^2 dx\, du$	1.3×10^{-5}	1.3×10^{-5}	$>1 \times 10^{38}$

Note. Maximum conservation errors (relative) during bump-on-tail simulations for the distribution and discretization listed in Table 7.

after using $\Phi^0(x) = 1$, $v = u/U$, and the Fourier orthogonality relation. Using the AW Hermites we know $v = \Psi^1(v)/\sqrt{2}$ so we may evaluate the integral $\int v\Psi_n(v)\,dv$ to yield

$$p(t) = \frac{m_e L U^2}{\sqrt{2}} f^{01}(t). \tag{48}$$

As in particle conservation, momentum is conserved during the X-shift because the $m = 0$ Fourier modes are not changed.

To assess the change in momentum during the AW Hermite V-shift, it is more convenient to use

$$\Delta p = \int [p(x, t_b) - p(x, t_a)]\,dx = \frac{m_e U^2}{\sqrt{2}} \int \left[f^1(x, t_b) - f^1(x, t_a) \right] dx. \tag{49}$$

Examining the AW Hermite V-shift equation (23), we find that $f^1(x, t)$ changes linearly in Δt because $\dot{f}^0(x, t) = 0$. In fact, the change in momentum during the AW Hermite V-shift is simply

$$\Delta p = \frac{\Delta t}{\sqrt{2}} \int m_e U^2 \dot{f}^1(x, t)\,dx \bigg|_{t=t_a} = \Delta t \int_{-L/2}^{L/2} E(x, t_a)\rho(x, t_a)\,dx, \tag{50}$$

where $\rho(x, t_a) \equiv q_e U f^0(x, t_a)$ is the charge density. Using Gauss' law and the periodicity of the fields, we find

$$\Delta p = \frac{\epsilon_o \Delta t}{2} \int_{-L/2}^{L/2} \frac{\partial E^2(x, t_a)}{\partial x}\,dx = 0. \tag{51}$$

Hence, *momentum is conserved* using the AW Hermite method. There is no RK4 error because $\dot{f}^1(x, t)$ is constant.

In contrast, the total momentum for the SW Hermite method is given by a sum over all of the odd Hermite modes,

$$p(t) = m_e L U^2 \sum_{\substack{n=1 \\ \text{odd}}}^{N_u} f^{0n}(t) I_{1n}, \tag{52}$$

where the coefficients I_{1n} may be generated recursively by $I_{1n} = \sqrt{n/(n-1)}\, I_{1,n-2}$ with $I_{11} = 2\pi^{1/4}$. The X-shift, as before, does not affect the $m = 0$ Fourier modes, so momentum is conserved during this step.

For the SW Hermite V-shift, we analyzed the conservation of momentum [29] by Taylor expanding $p(t_b)$ in Δt and evaluating the time-derivatives of momentum using Eq. (23) to find

$$\begin{aligned} \Delta p \propto\ & \Delta t I_{1,N_u-1} f^{N_u}(x, t_a) E(x, t_a) \\ & + \frac{\Delta t^2}{2} \left[I_{1,N_u-1} f^{N_u-1}(x, t_a) + I_{0,N_u-1} f^{N_u}(x, t_a) \right] E(x, t_a). \end{aligned} \tag{53}$$

If N_u is even then $I_{1,N_u-1} \neq 0$ and $\Delta p \sim O(\Delta t)$. But if N_u is odd then $I_{1,N_u-1} = 0$ and $I_{0,N_u-1} \neq 0$, so $\Delta p \sim O(\Delta t^2)$. Therefore, due to time-splitting, momentum is never conserved using the SW Hermite method. From bump-on-tail simulations to be shown later,

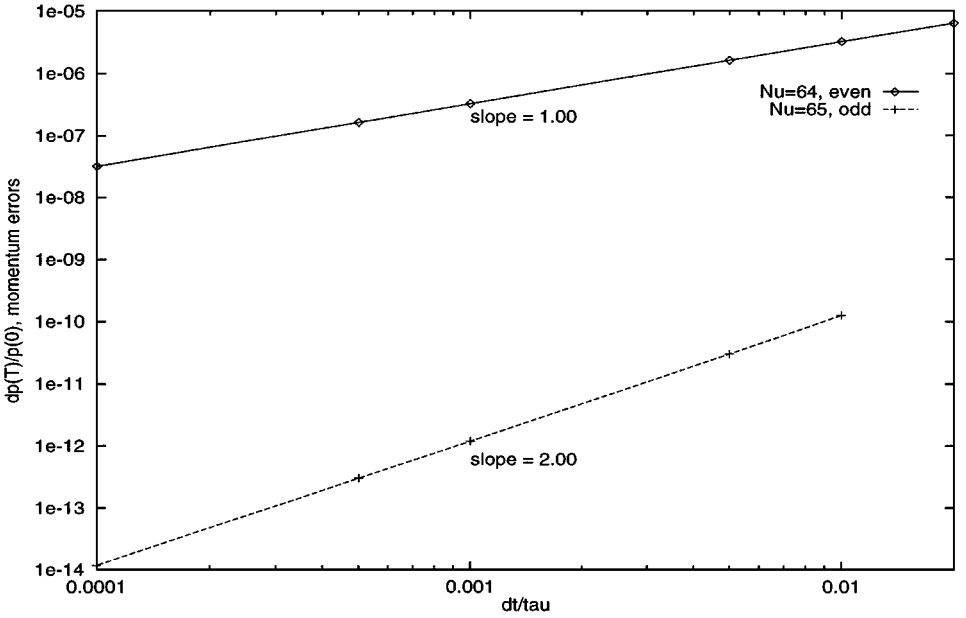

FIG. 3. Simulations results showing momentum conservation versus Δt for SW Hermite methods with even and odd Hermite expansion orders. The time is normalized by the plasma period "tau."

the relative change in momentum versus time (see Fig. 3) confirms that the errors scale like $O(\Delta t)$ for N_u even and $O(\Delta t^2)$ for N_u odd.

Note, if we have particle conservation by making N_u even, momentum conservation is limited to $O(\Delta t)$. If we get $O(\Delta t^2)$-accurate momentum conservation by making N_u odd, particle conservation is only $O(\Delta t)$. This is an annoying limitation of the SW Hermite method. However, as before, increasing the rate of spectral convergence will improve the conservation of momentum (see Eq. (53)) by making $f^{N_u}(x,t)$ and $f^{N_u-1}(x,t)$ smaller. Also, in cases in which the electric field is small or decreasing, the conservation of momentum can be very good.

In Table 3, we see that the Hermite methods have momentum conservation errors at round-off level during Landau damping simulations. During bump-on-tail simulations, the AW Hermite method has the lowest momentum conservation errors whereas momentum errors were about 6% when using the SW (even) Hermite method (see Table 4). It is important to note, however, that the even-order SW Hermite momentum conservation errors can be *reduced* several orders-of-magnitude by lowering the velocity-scale U (see Fig. 5); this momentum error reduction demonstrates one of the practical uses of improved spectral accuracy that can be gained through velocity-scaling.

Total Energy

The total energy of the system is the sum of the kinetic and potential energies,

$$H = \underbrace{\frac{m_e}{2}\int\int u^2 f(x,u,t)\,dx\,du}_{KE} + \underbrace{\frac{\epsilon_o}{2}\int |E(x,t)|^2\,dx}_{PE}. \tag{54}$$

The splitting technique decouples advection and acceleration, so we know that $\Delta KE = 0$ during the X-shift but is nonzero during the V-shift. In addition, because we hold $E(x,t) = E(x,t_a)$ during the V-shift, we know that $\Delta PE = 0$ during that step. Potential energy changes via spatial redistribution during the X-shift only. Now we need to calculate the changes in kinetic energy (KE) and potential energy (PE) for the AW and SW Hermite methods and determine whether or not $\Delta(\mathrm{KE}+\mathrm{PE}) = 0$. The $O(\Delta t^5)$ RK4 error will be neglected in this analysis of energy conservation because, as we will see below, the $O(\Delta t^3)$ splitting error dominates.

For the AW Hermite method, Eq. (54) may be evaluated to yield

$$H = \frac{L}{4} m_e U^3 [\sqrt{2} f^{02}(t) + f^{00}(t)] + \frac{\epsilon_o L}{2} \sum_m |E^m(t)|^2 \tag{55}$$

after using the substitutions $\Psi^0(v) = \Phi^0(x) = 1$ and $v^2 = \frac{1}{2}(\sqrt{2}\Psi^2 + \Psi^0)$. During the X-shift, the f^{0n} modes are invariant, so KE is constant.

During the AW Hermite V-shift, ΔKE may be more easily analyzed using the formula

$$\Delta\mathrm{KE} = \frac{m_e U^3}{4} \int \left[\sqrt{2}(f^2(x,t_b) - f^2(x,t_a)) + (f^0(x,t_b) - f^0(x,t_a))\right] dx, \tag{56}$$

where the subscript a denotes evaluation at "time" t_a, at the start of the V-shift. The second term in the integrand is zero during the AW Hermite V-shift because $\dot{f}^0(x,t) = 0$; i.e., particles do not free-stream. Taylor-expanding $f^2(x,t_b)$ in Eq. (56) and using Eq. (23) to evaluate the time-derivatives of $f^2(x,t_b)$ while holding $E(x,t_a) \equiv E_a$ constant, we find

$$\Delta\mathrm{KE} = \int \Delta t \left[\frac{q_e U^2 E_a}{\sqrt{2}} f^1(x,t_a)\right] + \frac{\Delta t^2}{2}\left[\frac{U q_e^2 E_a^2}{m_e} f^0(x,t_a)\right] dx \tag{57}$$

$$= -\epsilon_o \int \left(\Delta t E_a \dot{E}_a - \frac{\Delta t^2}{2}\omega_{pe}^2(x) E_a^2\right) dx, \tag{58}$$

where we have identified the local plasma frequency $\omega_{pe}^2(x) = U q_e^2 f^0(x,t_a)/\epsilon_o m_e$ and $\dot{E}_a = q_e U^2 f^1(x,t_a)/\sqrt{2}$. The higher-order terms are exactly zero because $\dot{f}^0(x,t) \equiv 0$ during the AW Hermite V-shift. We know that during the V-shift, $\ddot{E}(x,t) = -\omega_{pe}^2 E(x,t)$ is satisfied, so

$$\Delta\mathrm{KE} = -\epsilon_o \int \left(\Delta t E_a \dot{E}_a + \frac{\Delta t^2}{2} E_a \ddot{E}_a\right) dx \tag{59}$$

with no higher-order terms.

The total change in PE is the sum of the individual changes in potential energy (PE) during the entire time-step, accounted for individually and written

$$\Delta\mathrm{PE} = \frac{\epsilon_o}{2} \int \underbrace{\left(E_{\Delta t}^2 - E_b^2\right)}_{\text{X-shift}} + \underbrace{\left(E_b^2 - E_a^2\right)}_{\text{V-shift}} + \underbrace{\left(E_a^2 - E_0^2\right)}_{\text{X-shift}} dx, \tag{60}$$

where we have used the notation $E(x, t+\Delta t) = E_{\Delta t}$, $E(x,t_b) = E_b$, etc. During the X-shifts, we can Taylor-expand $E_{\Delta t}^2$ and E_0^2 in time and cast them in terms of E_b^2 and E_a^2,

respectively, so that

$$E_{\Delta t}^2 = E_b^2 + \Delta t E_b \dot{E}_b + \frac{\Delta t^2}{4}\left(E_b \ddot{E}_b + (\dot{E}_b)^2\right) + O(\Delta t^3) \tag{61}$$

$$E_0^2 = E_a^2 - \Delta t E_a \dot{E}_a + \frac{\Delta t^2}{4}\left(E_a \ddot{E}_a + (\dot{E}_a)^2\right) + O(\Delta t^3). \tag{62}$$

If we recall that during the V-shift, $E_b = E_a$, $\dot{E}_b = \dot{E}_a + \Delta t \ddot{E}_a + O(\Delta t^2)$, and $\ddot{E}_b = \ddot{E}_a + O(\Delta t)$, then the total change in PE reduces to

$$\Delta \mathrm{PE} = \epsilon_o \int \left(\Delta t E_a \dot{E}_a + \frac{\Delta t^2}{2} E_a \ddot{E}_a\right) dx + O(\Delta t^3) \tag{63}$$

which is nearly canceled by the changes in KE shown in Eq. (59), making the change in total energy $O(\Delta t^3)$. The splitting scheme limits energy conservation in the AW Hermite method to $O(\Delta t^3)$ by accelerating the particles with the wrong E-field during the V-shift; energy conservation for the AW Hermite method is plotted versus time-step Δt in Fig. 4 with data taken from simulations to be shown later.

For the SW Hermite method, we may re-write (54) to find that the total energy of the system is given by

$$H = \frac{L m_e U^3}{2} \sum_{\substack{n=0 \\ \text{even}}}^{N_u} (2n+1) I_{0n} f^{0n}(t) + \frac{\epsilon_o L}{2} \sum_m |E^m(t)|^2, \tag{64}$$

where we used $\int v^2 \Psi_n(v)\, dv = (2n+1) I_{0n}$. As before, KE does not change during the

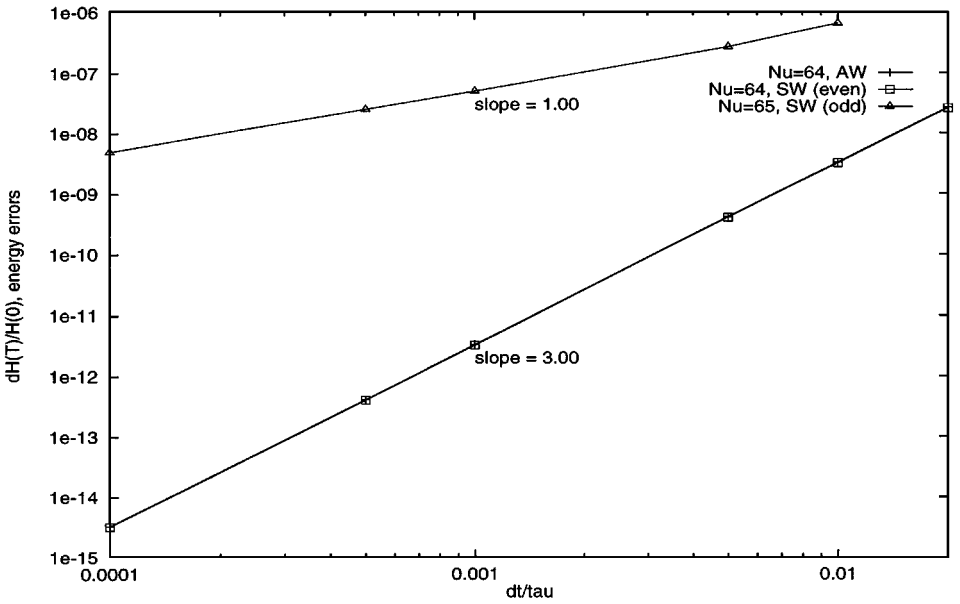

FIG. 4. Simulation results showing energy conservation versus Δt from AW and SW Hermite methods (both even and odd expansion order N_u are shown). The AW Hermite and even SW Hermite data overlap.

X-shift. During the V-shift, the change in kinetic energy is

$$\Delta \mathrm{KE} = \dot{\mathrm{KE}}|_a \Delta t + \ddot{\mathrm{KE}}|_a \frac{\Delta t^2}{2} + O(\Delta t^3), \tag{65}$$

where a represents evaluation of the time-derivatives at "time" t_a before the V-shift. Taking the time-derivative of KE and using the SW Hermite V-shift equation (23), we find

$$\dot{\mathrm{KE}} = \frac{m_e U^3}{2} \sum_{\substack{n=0 \\ \text{even}}}^{N_u} (2n+1) I_{0n} \int f^n(x,t)\, dx \tag{66}$$

$$= -\epsilon_o \int E(x,t_a) \dot{E}(x,t)\, dx - \underbrace{q_e U^2 \frac{2N_u+3}{2} I_{1,N_u} \int E(x,t_a) f^{N_u}(x,t)\, dx}_{\text{truncation error}}. \tag{67}$$

Higher-order time derivatives of the truncation error term are also proportional to I_{1,N_u}. If N_u is even, we find

$$\Delta \mathrm{KE} = -\epsilon_o \int E_a \dot{E}_a \Delta t + E_a \ddot{E}_a \frac{\Delta t^2}{2} + \dddot{E}_a \frac{\Delta t^3}{6}\, dx + O(\Delta t^4). \tag{68}$$

The $O(\Delta t^3)$ term does not cancel the $O(\Delta t^3)$ term in ΔPE (see Eq. (63)) because the E-field is held constant during the V-shift; hence, the error in energy conservation for N_u even is $O(\Delta t^3)$. However, if N_u is odd, then the truncation error in Eq. (67) is $O(\Delta t)$ and the error in energy conservation for the SW Hermite method is given by

$$\Delta \mathrm{H} = \Delta t q_e U^2 \left(\frac{2N_u+3}{2} \right) I_{1,N_u} \int E(x,t_a) f^{N_u}(x,t)\, dx. \tag{69}$$

Once again, we have an important difference between even-order and odd-order expansions of SW Hermites; energy conservation versus expansion order and Δt during simulations is shown in Fig. 4. Improved energy conservation can be obtained by reducing the magnitude of $f^{N_u}(x,t)$ with a spectrally accurate SW (odd-order) Hermite representation; however, the splitting error dominates the even-order SW Hermite energy conservation errors shown in Fig. 5, so that velocity scaling has little or no affect. An unsplit time-stepping scheme could possibly find enhanced energy conservation through improved spectral accuracy.

A summary of the conservation properties for the AW, even-order SW, and odd-order SW hermite methods is given in Table 2. The AW Hermite method conserves particles and momentum, limited only by the RK4 scheme; energy conservation error for the AW Hermite method is dominated by the splitting scheme. The SW Hermite method, on the other hand, is limited primarily by truncation in the V-shift equation (see Eq. (23)). The even-order SW Hermite expansions obtain the best conservation for particles and energy because these quantities are determined by the even Hermite coefficients. Similarly, the odd-order SW Hermite method obtains the best conservation for momentum, which is determined by odd Hermite coefficients. This even versus odd conservation trade-off, which is familiar from PIC methods [4], is an annoying limitation of the SW Hermite schemes developed here.

Another important quantity conserved by the SW Hermite method but not discussed above is integral $J = \iint f^2(x,u,t)\, dx\, du$. Weighted residuals methods based on SW Hermites naturally conserve this quantity while, in contrast, AW Hermite methods cannot [32].

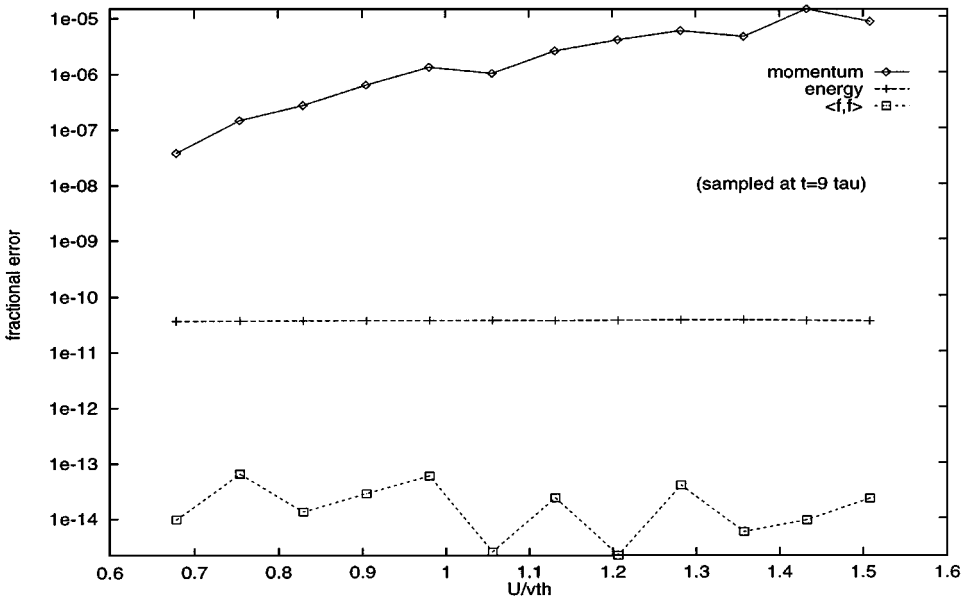

FIG. 5. Conservation of momentum, energy, and $\int\int f^2$ is plotted versus normalized velocity scale U/v_{th}, showing two orders-of-magnitude reduction in momentum errors with decreasing velocity scale length. Energy and $\int\int f^2$ errors are not noticeably affected for the SW (even) Hermite method.

The maximum J-conservation errors are tabulated in Tables 3 and 4. While errors in J are on the order of 10^{-14} for the even and odd SW Hermite methods, error in J for the AW Hermite method are at or above 10^{12}. In fact, during bump-on-tail simulations shown below, the AW Hermite method became *numerically unstable* after the quantity J became large. The inherent lack of stability in the AW Hermite method is due to its inability to conserve J.

SIMULATIONS

By assessing the abilities of the Fourier–Hermite (FH) algorithms to model well-known linear plasma physics and by understanding their numerical limits we can gain confidence in their ability to likewise model nonlinear phenomena accurately and efficiently. In this section, we will test and compare these FH methods by modeling the electrostatic evolution resulting from (a) an initially perturbed, yet stable, equilibrium Maxwellian velocity profile and (b) an initially perturbed and unstable equilibrium bump-on-tail velocity profile.

Landau damping and growth of some electrostatic waves, two phenomena in collisionless plasmas governed by similar physical mechanisms are the result of a resonant coupling between the phase velocity of an electrostatic wave and the *local* velocity profile of charged particles. Oscillation frequencies for a stimulated electrostatic mode, on the other hand, are determined by the *global* velocity profile. Therefore, optimal spectral representations of the velocity distribution, which can be obtained by proper choice of a velocity scaled Hermite basis function, will produce good agreement to linear theory with reduced computational effort, i.e. fewer coefficients stored for equivalent accuracy requirements, as compared to unscaled Hermite representations. In both sets of simulations, fidelity of the solutions will

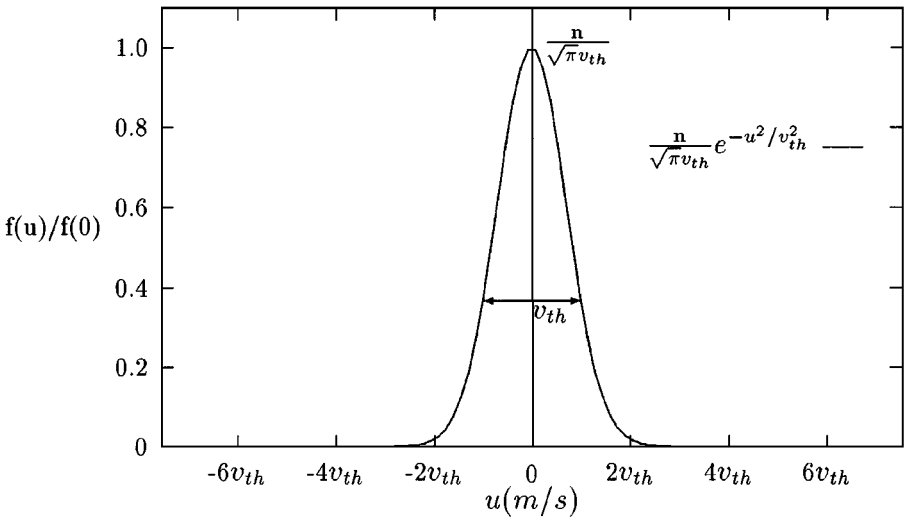

FIG. 6. A Maxwellian velocity profile.

be established by comparisons to linear kinetic theory and to the results of one-dimensional (1d-1v) PIC simulations using ES1 [4]. In order to demonstrate the long-time stability and accuracy of the method, we also compare our method to the results of a "method of characteristics" Vlasov method [21] similar to the method of Cheng and Knorr [9].

Linear Landau Damping

The initial input distribution to be used is a simple Maxwellian (see Fig. 6) in velocity space with thermal velocity v_{th},

$$f(x, u, 0) = \frac{g(x)}{\sqrt{\pi}v_{th}} \exp\left[-\frac{u^2}{v_{th}^2}\right], \tag{70}$$

and a cosinusoidal profile in space,

$$g(x) = n_o[1 + \epsilon \cos(Kx)], \tag{71}$$

characterized by the number density n_o, perturbation amplitude ϵ, and a wavenumber $K = 2\pi k/L$ for some stimulated integer mode number k. In these simulations, we will analyze an electron plasma, charge-neutralized by setting $E^0(t)$ Fourier mode to zero.

A representative example of the AW and even-order SW Hermite simulation results is shown in Fig. 7, illustrating the damping of $|E^1(t)|$ with time. The time coordinate has been normalized by the plasma period, $\tau_{pe} = 2\pi/\omega_{pe}$, where $\omega_{pe} = 1.0\ \mathrm{s}^{-1}$ in these Landau damping simulations.

In the simulation results shown, no attempt to optimize U was made (i.e., $U = 1$) so we notice in Fig. 7 that after several oscillations the linear damping ceases and is followed by a recursion of the E-field. Landau damping is due to phase-mixing (destructive interference) of the infinite number of oscillation modes that are supported in a real plasma [33]. Because a discrete velocity grid cannot support a continuum of phase velocities, discrete Vlasov methods are unable to indefinitely mimic this process. The time at which destructive interference of the oscillating modes ceases is known as the *recursion time*

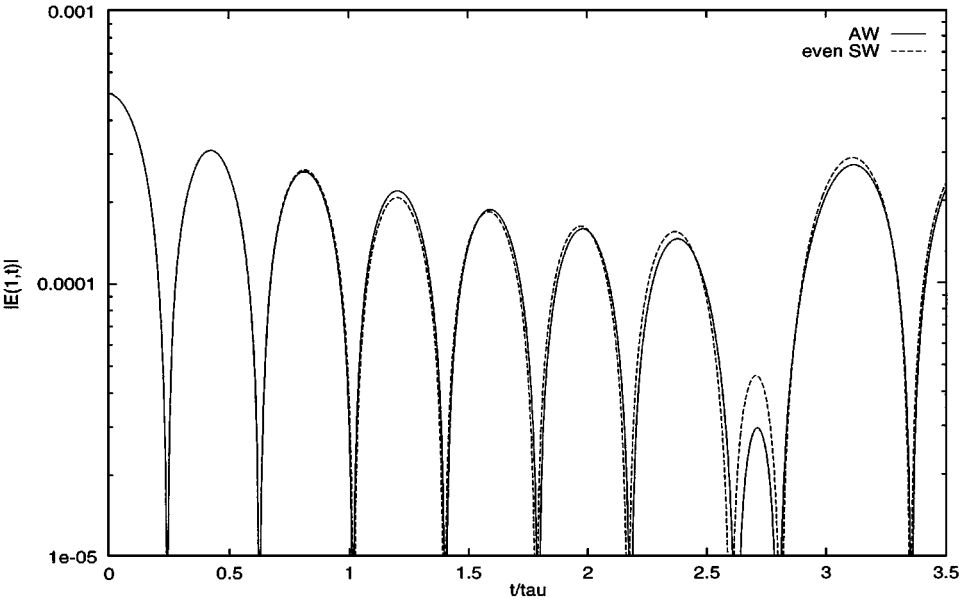

FIG. 7. Comparison of Landau damping results using AW and SW (even) Hermite methods, demonstrating the damping of an electrostatic wave versus t/tau, where tau $= \tau_{pe} = 2\pi/\omega_{pe}$. These simulations were unscaled, i.e. U $= 1$, thus yielding a very short recursion time of about $2.5\tau_{pe}$.

[11, 14, 26] and is given approximately by $\tau_{recur} \sim \pi/(K\,\Delta u)$, where Δu is the velocity resolution of phase-space grid and K is the wavenumber of the stimulated electrostatic wave.

The recursion time, which is inversely proportional to the velocity resolution, can be extended by (a) increasing the Hermite expansion order N_u or (b) decreasing the velocity scale U. We recall that $\Delta u \sim U/\sqrt{N_u}$ and so the recursion time scales as

$$\tau_{recur} \sim \frac{\pi\sqrt{N_u}}{KU}. \tag{72}$$

Decreasing the velocity scale U lengthens the recursion time in a linear fashion yet does not increase the computational effort. Increasing the Hermite expansion order N_u, on the other hand, only increases recursion time like $\sqrt{N_u}$ while increasing the computational workload like N_u. Although lowering U will eventually lead to poor modeling of the tails of the distribution, moderate reduction of U can lengthen recursion time significantly (see Fig. 8).

In addition to lengthening recursion time, proper selection of the velocity scale U can enhance the agreement of simulated damping with linear Landau damping theory. This fact is confirmed in Figs. 9 and 10 for the AW and SW Hermites, respectively. In these plots, the errors in frequency and growth rate as compared to linear Landau damping theory [1] are shown versus velocity scale U/v_{th}. Solution of the dispersion relation for a Maxwellian velocity profile (see Table 5) yielded a frequency $\omega_{theory} = 1.28525\ \mathrm{s}^{-1}$ and damping rate $\gamma_{theory} = -0.066237\ \mathrm{s}^{-1}$ for the stimulated mode $k = 1$. The phase velocity of the damping electrostatic wave, in this case, is $v_\phi = 0.2046$ m/s. From these figures, we see that the optimal range of velocity scales for the AW Hermite method is $0.8v_{th} < U < 1.2v_{th}$, yielding dispersion errors near 1% in the damping rate γ and less than 0.05% in the oscillation

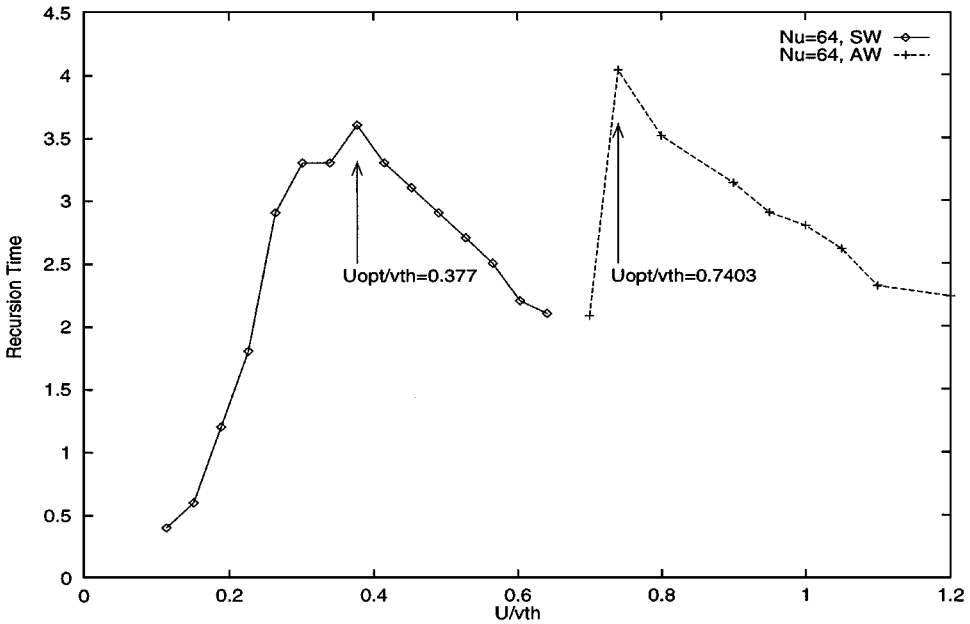

FIG. 8. Lengthening of the recursion time over which linear Landau damping can be modeled is accomplished by proper selection of the velocity scale U.

frequency ω. The optimal range for the SW Hermite method is $0.3v_{th} < U < 0.6v_{th}$, with dispersion errors very similar to those found using the AW Hermite method. The lower bound on the $U_{optimal}$ range is determined by Eq. (20) for the AW Hermite method, whereas the lower $U_{optimal}$ bound for the SW Hermite method is determined by $u_{max} \approx v_\phi$.

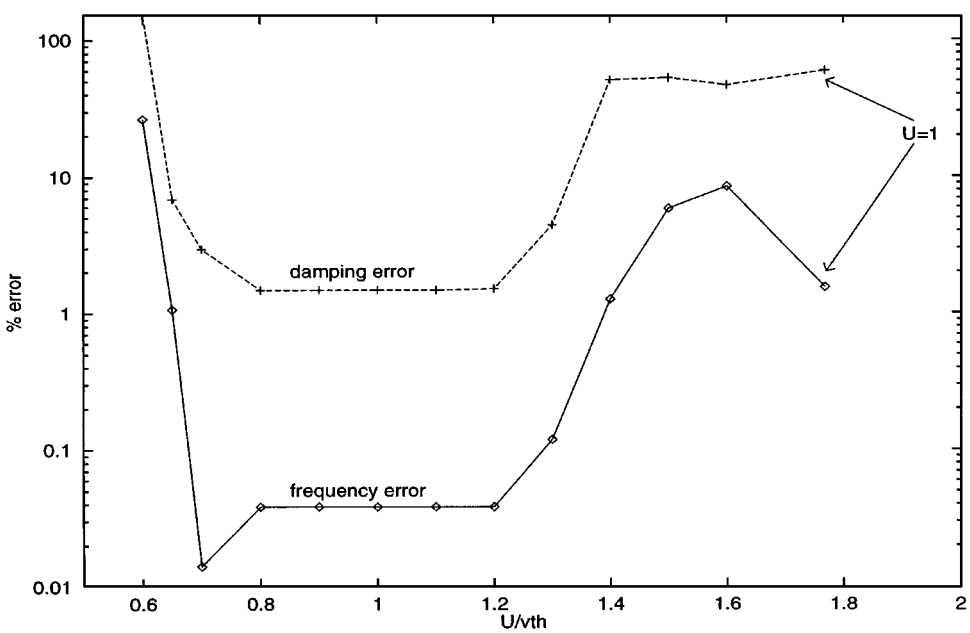

FIG. 9. A variable velocity-scale U can greatly improve the agreement between oscillation frequencies and damping rates generated by AW FH simulations and those expected from the linear Landau damping theory. To retain high accuracy *and* long recursion time, we find the optimal value lies near $U = 0.8v_{vth}$.

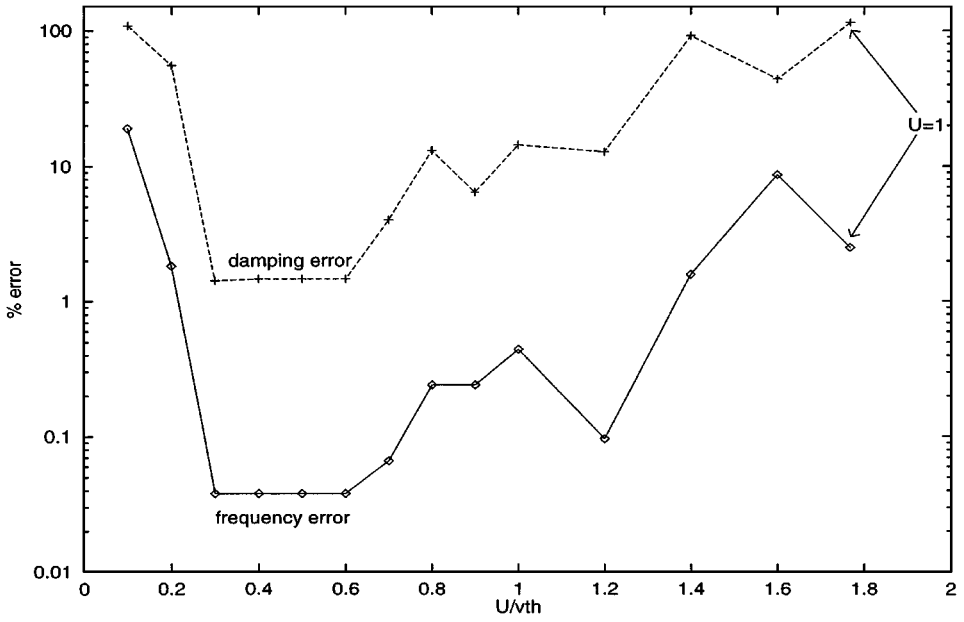

FIG. 10. A variable velocity-scale U can greatly improve the agreement between oscillation frequencies and damping rates generated by SW FH simulations and those expected from the linear Landau damping theory. The optimal value lies near $U = 0.4v_{vth}$.

The unscaled Landau damping simulations using $U = 1$ with 64 Hermite functions, also shown in Figs. 9 and 10, yielded dispersion errors between 10 and 100%. These simulations demonstrate that a proper choice of velocity scale U can yield *orders of magnitude* improvement in modeling linear Landau damping when using Hermite basis functions. Velocity scaling of Hermites has not been utilized before in the numerical simulation of the nonlinear Vlasov–Poisson equations.

TABLE 5
Landau Damping Simulation Input

Parameter	Symbol	Value used [units]
Number of PIC particles	N_p	4k-128k
Number density	n_o	1.0 [sheets/m]
Thermal velocity	v_{th}	0.56568542 [m/s]
Electron mass	m_e	1.0 [kg]
Electron charge	e	−1.0 [C]
Permittivity	ϵ_o	1.0 [F/m]
Spatial resolution	N_x	64 (FH) or 128 (PIC)
Hermite velocity resolution	N_u	64
Temporal resolution	Δt	$7.9974 \times 10^{-4}[\tau_{pe}]$
Spatial length	L	2π [m]
velocity scale	U/v_{th}	Variable
Perturbation amplitude	ϵ	0.001
Perturbation mode number	k	1

Note. Standard input values for ES1 and FH comparison simulations of Landau damping in an electron plasma with a Maxwellian velocity profile.

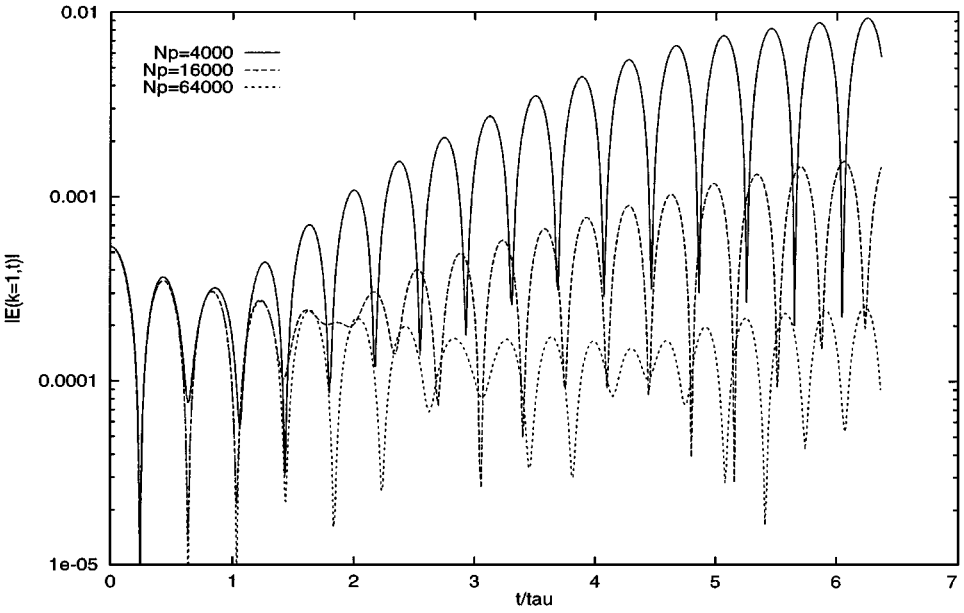

FIG. 11. PIC (ES1) results showing Landau damping of the stimulated electric field amplitude with time versus particle number, ranging from 4000 to 64000 particles. Damping of the electric field continues until the multiple-beam instability dominates. Here, the perturbation parameter is $\epsilon = 0.001$.

Conservation errors for both AW and SW method were relatively low. Using the velocity-scale values of $U/v_{th} = 0.4$ (SW) and $U/v_{th} = 0.9$ (AW), the maximum relative errors were calculated and tabulated in Table 3.

Landau Damping Comparisons

Using a standard and well-documented PIC code ES1 [4] and the Maxwellian beam input "LANDAU.INP" provided with that software, we generated Landau damping results as shown in Fig. 11. For a fair comparison of accuracy, our FH simulations used the same input distribution and similar velocity resolutions. The FH simulations used $N_x = 64$ Fourier modes and the PIC simulations used $N_x = 128$ spatial grid points, so the PIC simulations in fact had a greater spatial resolution. The input deck for the PIC/FH comparisons is shown in Table 5.

Figure 11 shows how the variation in the PIC E-field evolution depends on the number of particles in the system (ranging from 4000 to 64000 macroparticles). Note that there is a numerical multiple-beam instability [4], due to the inability of PIC codes to perfectly load an initial Maxwellian velocity profile. In PIC simulations, a Maxwellian velocity distribution is often approximated by initially prescribing several monoenergetic beams of macroparticles; each *beamlet*, having a specific velocity and density, contributes to the initial velocity profile in a way that approximates a Maxwellian (this is called a "cold start"). Macroparticle velocities can be then randomized about their mean beamlet velocity in order to reduce the artificial multibeam instability by filling in the phase-space holes (this is called a "warm start"). However, the "warm start" has the difficulty in that this initial randomization (numerical noise) may overwhelm the initial electostatic perturbation to be studied. In the PIC simulations shown here, a "cold start" is used.

TABLE 6
Landau Damping Results

Method	$\omega + i\gamma$	% error
Linear theory	$1.28525 - i0.066237$	0.0
PIC, $N_p = 16000$	$1.403 + i0.0110$	$9.2 + i116.6$
PIC, $N_p = 32000$	$1.470 - i0.0103$	$14.4 + i84.5$
PIC, $N_p = 64$k	$1.290 - i0.0541$	$0.40 + i18.3$
PIC, $N_p = 128$k	$1.289 - i0.0657$	$0.33 + i0.75$
AW Hermite	$1.285 - i0.0672$	$0.038 + i1.464$
SW Hermite (even)	$1.285 - i0.0672$	$0.038 + i1.464$

Note. Comparison of the Landau damping dispersion errors between a PIC code and the Hermite methods. The real portion of the percent error corresponds to frequency, ω; the imaginary portion corresponds to the damping rate, γ. Sampling errors (systematic errors in measuring omega and gamma) were approximately $\pm 0.26\%$ for all cases.

Table 6 shows comparisons of PIC and FH linear damping results with linear theory. The frequencies ω and growth rates γ in these tables were determined by finding the peaks of $|E^k|$ from the numerical run, determining the frequency of these peaks, and then their damping rate. There are therefore errors in ω and γ (about 0.3%) due to the sampling of the data in time. The FH method, using 4096 unknowns, yielded results more accurate than a 32000-particle PIC simulation. The simulation time for the FH method was about 55 s on a dedicated IBM RS6000 39H workstation; for the 32000 particle PIC simulation, it was 165 s.

Additionally, the PIC Landau damping is limited by the artificial multibeam instability; to see long-time Landau damping, the required particle number in PIC simulations must increase as the perturbation parameter ϵ decreases. The FH methods do not suffer this difficulty.

The FH method, which is limited by recursion but not by the multiple-beam instability, can exhibit long-time Landau damping for a wider range of perturbation amplitude ϵ than does PIC (see Figs. 12 and 13). For this reason, a spectral kinetic method is superior to PIC for the study of warm plasma dynamics in cases where a small perturbation amplitude ϵ is physically relevant.

To further validate the scaled FH method presented here, we directly compared the long-time nonlinear Landau damping of a monochromatic wave in an electron plasma to results presented in [21]. In Fig. 14, we show the initial damping, saturation, and amplitude oscillation of the $k = 3$ electrostatic mode versus $\omega_{pe}^{-1} t$ up to $T = 300\omega_{pe}^{-1}$. In our simulations using the scaled SW FH method with $N_x = 64$ Fourier and $N_u = 160$ Hermite functions (10240 unknowns), we measured the frequency, damping rate, and recursion time to be $\omega = 1.160$, $\gamma = -0.0127$, and $\tau_{recur} \approx 250\omega_{pe}^{-1}$, respectively (here, $K = 0.3$ and $\omega_{pe} = 1$). The theoretical values for this electrostatic mode are $\omega = 1.1598$ and $\gamma = -0.0125$, yielding an overall error of $0.017\% + 1.6i\%$. The expected recursion time is $255\omega_{pe}^{-1}$. A velocity scale length of $U = 0.225 v_{th}$ was selected in order to maximize the velocity resolution near the predicted phase velocity $v_{phase}/v_{th} = 3.866$. Relative errors in particle, momentum, and energy conservation were at most 4×10^{-15}, 10^{-14}, and 2×10^{-6}, respectively. The integral of f^2 never changed by more than 10^{-6} during the entire simulation.

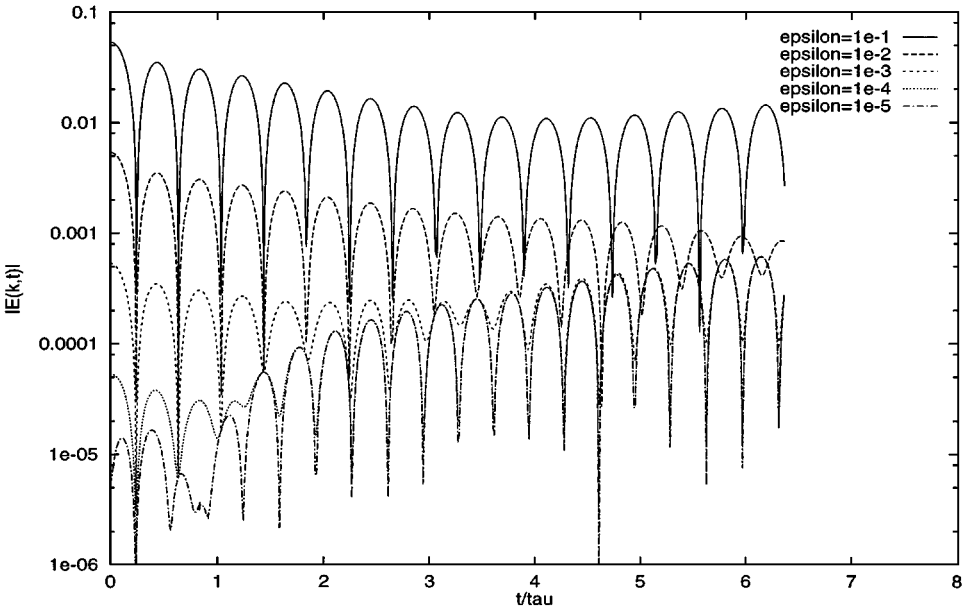

FIG. 12. PIC (ES1) results showing Landau damping of the stimulated electric field amplitude with time versus initial perturbation amplitude, ϵ.

Previous comparisons of Hermite-based methods [21] required 1600 AW Hermite polynomials in order to match the accuracy that was found using a method of characteristics [9, 21] with 128 grid points in velocity. However, with the proper velocity scaling, we only needed to use 160 SW Hermite functions. In fact, in simulations where $v_{phase}/v_{th} < 1$, even

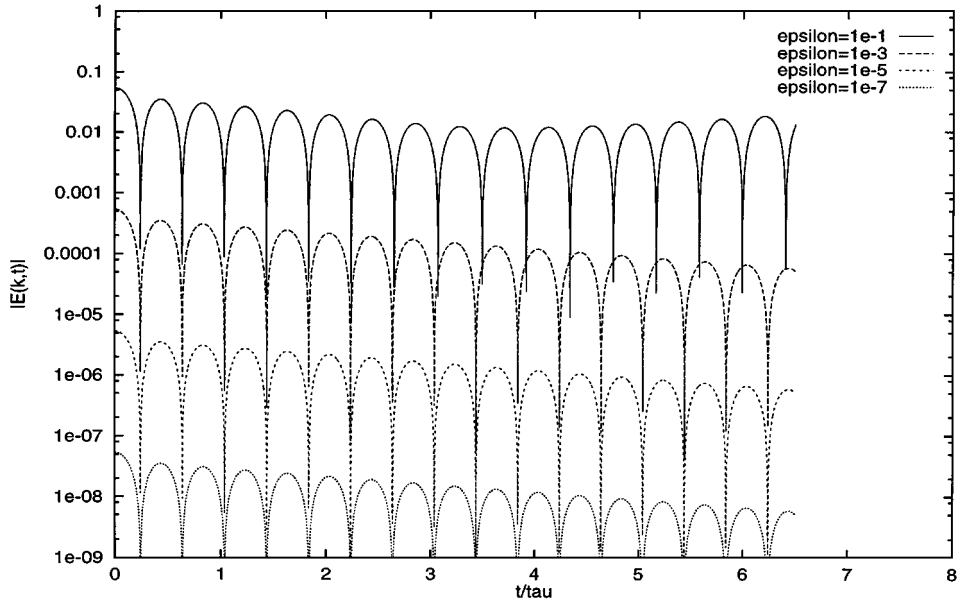

FIG. 13. Fourier–Hermite simulations can demonstrate linear Landau damping induced by small perturbations ϵ and are not affected by the multibeam instability. This may allow the modeling of initially low-noise systems.

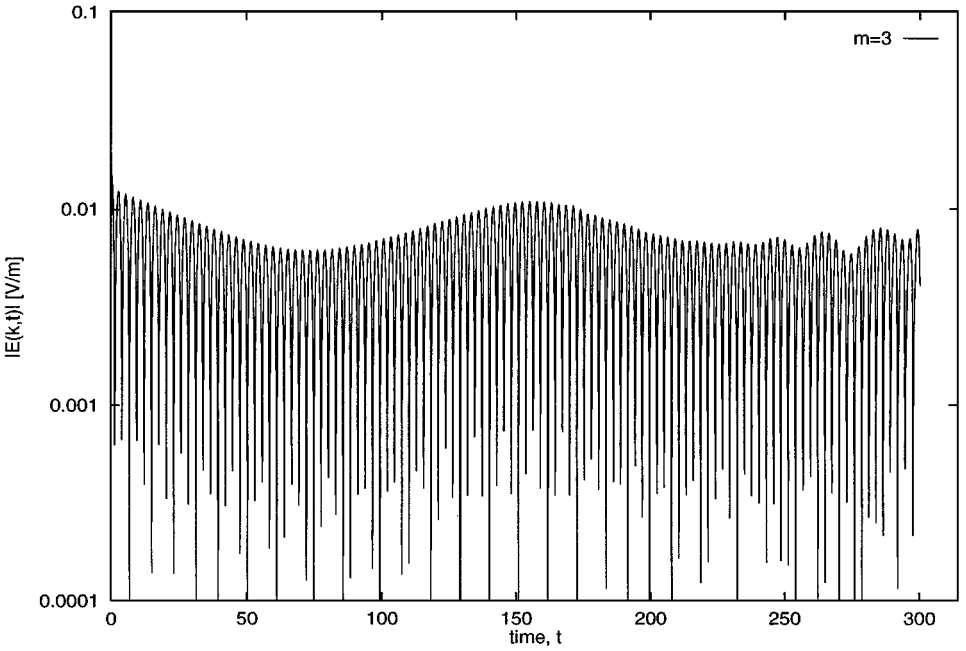

FIG. 14. For direct comparison to results shown in Gagne and Shoucri [21], a SW FH simulation of long-time Landau damping is shown, demonstrating the long-time accuracy and stability of the method. Previous unscaled Hermite-based methods required 1600 polynomials to obtain a similar recursion time of $255\omega_{pe}^{-1}$, whereas our scaled method required only 160 Hermite functions.

fewer Hermite polynomials would be needed because the resolution is higher near $u = 0$ for fixed N_u and U/v_{th}. With this in mind, Hermite-based methods are only comparable to other Vlasov methods when properly *scaled*; in low v_{phase} simulations, the Hermite methods can be superior.

Comparisons to PIC: Bump-on-Tail Instability

In this section, the initial input distribution function is a bump-on-tail (BOT) velocity profile (i.e., a Maxwellian plus a high-energy warm beam; see Fig. 15) written as

$$f(x,u,0) = g(x)\left[\frac{n_p}{\sqrt{\pi}v_{th,p}}\exp\left(-\frac{u^2}{v_{th,p}^2}\right) + \frac{n_b}{\sqrt{\pi}v_{th,b}}\exp\left(-\frac{(u-v_{d,b})^2}{v_{th,b}^2}\right)\right], \quad (73)$$

where the main "plasma" distribution is defined by the number density n_p and thermal velocity $v_{th,p}$. The "bump" distribution is defined by the number density n_b, the thermal velocity $v_{th,b}$, and the drift velocity $v_{d,b}$. In these simulations, we will again analyze a background-neutralized electron plasma, with its physically relevant quantities defined in Table 7. The initial spatial dependency $g(x)$ will again have cosinusoidal form defined previously in Eq. (71), where ϵ is the perturbation amplitude, k is the mode number stimulated, and L is the system length. Only one mode number k will be stimulated in any simulation.

Figure 16 shows a representative phase space plot of the distribution function soon after saturation of the electrostatic field; the resonant traps or "cat's-eyes" are clearly visible.

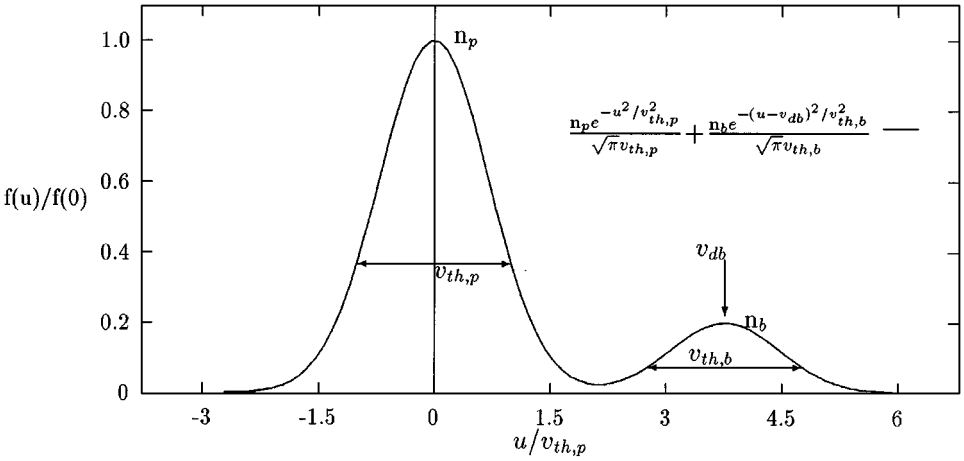

FIG. 15. A bump-on-tail (BOT) velocity profile.

This simulation used the SW Hermite method with $N_x = 64$, $N_u = 64$, and an optimal scale length of $U/v_{th} = 0.4$. Figure 17 provides a quantitative view of the importance of proper scaling, showing for both SW and AW Hermite methods, the error (modulus of the difference from linear theory) in the complex time constant $(\omega + i\gamma)$ as a function of scale length U. In Fig. 18 we compare the E-field growth as computed by the optimized SW Hermite method to that computed by PIC for varying numbers of particles. The PIC results are clearly converging towards the SW Hermite results. This not only validates the Hermite method, but it also demonstrates that PIC requires very many more unknowns to achieve the accuracy of the spectral method.

TABLE 7
Bump-on-Tail Simulation Input

Parameter	Symbol	Value used [units]
Number of PIC particles	N_p	64000–1024000
Number densities	n_p	1.0 [sheets/m]
	n_b	0.01 [sheets/m]
Thermal velocities	$v_{th,p}$	0.28284271 [m/s]
	$v_{th,b}$	7.0710678e-2 [m/s]
Drift velocity	$v_{d,b}$	1.0 [m/s]
Electron mass	m_e	1.0 [kg]
Electron charge	e	-1.0 [C]
Permittivity	ϵ_o	1.0 [F/m]
Spatial resolution	N_x	64 (FH) or 128 (PIC)
Velocity resolution	N_u	64 or 65
Temporal resolution	Δt	$7.9974 \times 10^{-3}[\tau_{pe}]$
Spatial length	L	20π [m]
Velocity scale	U/v_{th}	variable
Perturbation amplitude	ϵ	1.0×10^{-4}
Perturbation wavenumber	k	10

Note. Standard values for comparison of ES1 and FH bump-on-tail simulations.

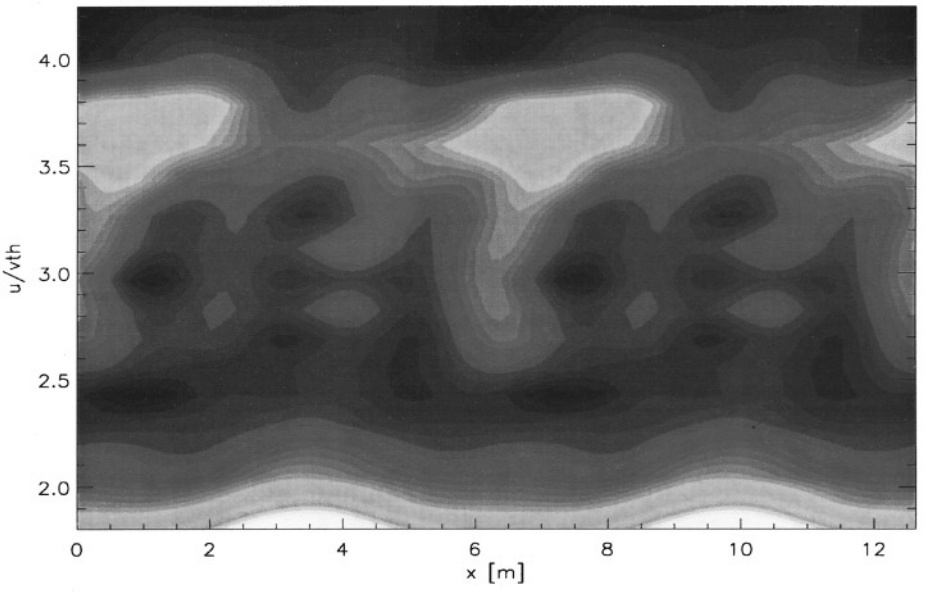

FIG. 16. A plot of $f(x, u, t)$ contours in phase-space (x, u) at $\omega_{pe}t = 32\pi$. The "cat's eye" phase-space structures are moving at $v_{phase} = 3.5v_{th}$. In this bump-on-tail simulation, we used the SW Hermite method with $k = 2$, $N_x = N_u = 64$, and $U/v_{th} = 0.4$.

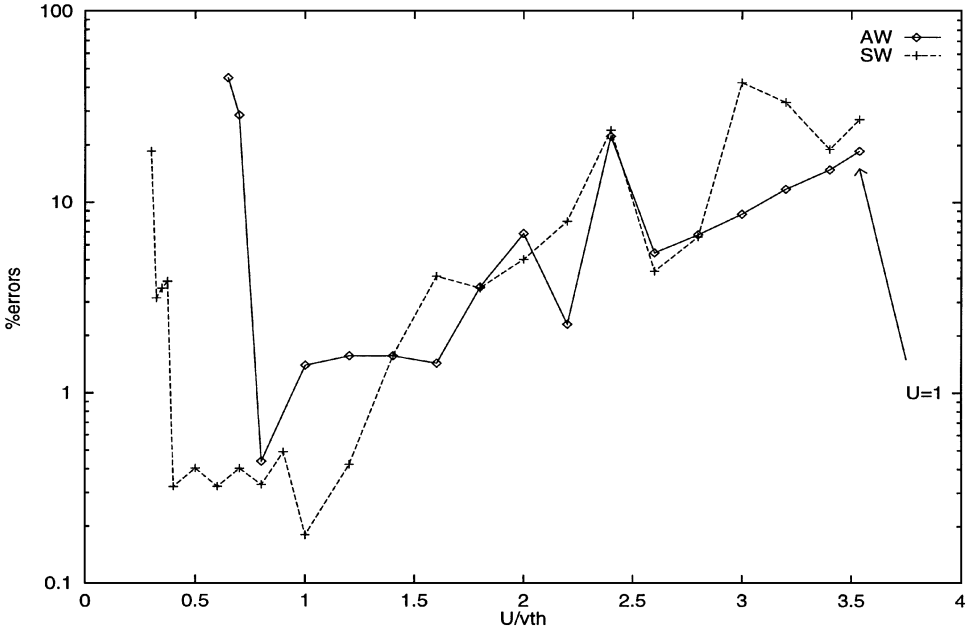

FIG. 17. A comparison of AW versus SW (even order) Hermite methods, varying the velocity scale U/v_{th}. Optimal U/v_{th} ranges from 0.4 to 1.3 for the SW Hermites; for the AW Hermite method, a narrow optimal range lies near $U/v_{th} = 0.8$. These results are taken from the BOT simulations described in this article.

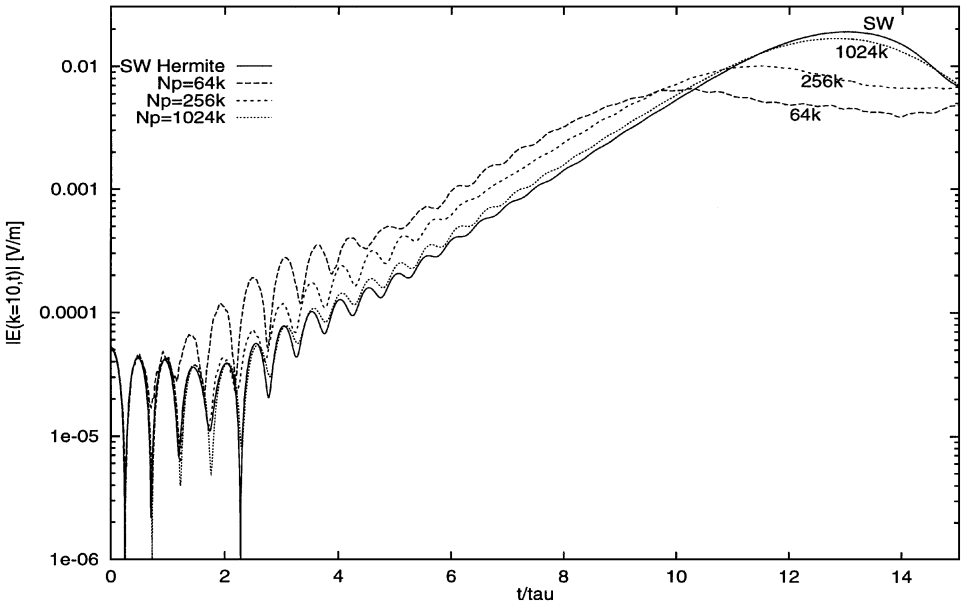

FIG. 18. PIC simulations of the BOT instability are shown to converge to the Fourier-SW Hermite results as the number of PIC particles increases from 16000 to 1024000. The FH simulation was completed over 6 times faster than the 64000 particle PIC simulation.

We may clearly see that the Hermite methods are superior to the PIC methods for warm plasma simulations by comparing both quantitatively to linear theory. In Table 8 we see that the PIC code can predict the oscillation frequency of the electrostatic mode to within 1% of linear theory, and as well as the Hermite methods, by using about 256000 particles. However, the growth rate γ of the mode is still poorly modeled by PIC. Even using over 500000 particles, the error in the PIC growth rate is still almost 3%. In contrast, the SW Hermite schemes, using 4096 unknowns, predicted both ω and γ to within 1% of linear theory. The PIC simulation with 64000 particles had a runtime of 5.47 minutes on a dedicated

TABLE 8
Bump-on-Tail Results

Method	$\omega + i\gamma$[1/sec]	% error
Linear theory	$0.9295028 + i0.1084353$	0.0
PIC, $N_p = 64000$	$0.9363793 + i0.0898235$	$0.740 + i17.2\%$
PIC, $N_p = 128000$	$0.9326943 + i0.0940847$	$0.343 + i13.2\%$
PIC, $N_p = 256000$	$0.9286062 + i0.1010277$	$0.097 + i6.83\%$
PIC, $N_p = 512000$	$0.9286057 + i0.1053760$	$0.097 + i2.82\%$
FH, SW (even)	$0.9288249 + i0.1076992$	$0.073 + i0.68\%$
FH, SW (odd)	$0.9288249 + i0.1076980$	$0.073 + i0.68\%$
FH, AW	$0.9289522 + i0.1114054$	$0.059 + i2.74\%$

Note. Comparison of the BOT dispersion errors between a PIC code and the Hermite methods. Frequencies and growth rates were taken from E-field oscillations between 6 and $10\tau_{pe}$. Sampling errors are approximately 0.26% for all cases.

IBM RS6000. The SW FH simulation had a runtime of 0.89 minutes on the same machine *and* yielded much higher accuracy.

The AW Hermite method, while performing better than PIC at earlier simulation times, did not perform as well as the SW Hermite method in the long run. Specifically, the AW Hermite method became unstable at long times due to poor conservation of the integral of f^2; the quantity $\int\int f^2\,dx\,du$ rose exponentially throughout the simulation to about 6000% after the saturation of the E-field. During the time of frequency and growth rate measurements (linear growth), the errors in $\int\int f^2\,dx\,du$ ranged from 20% up to 400%. Although the $\int\int f^2\,dx\,du$ error is contained primarily in the higher order Hermite coefficients which are not directly used in calculating the E-field, the high order Hermite modes grow exponentially and render first the distribution function and then eventually the E-field useless. The inability of the AW Hermite method to conserve $\int\int f^2\,dx\,du$ makes the method unsuitable for long-time simulations.

The SW Hermite method, in contrast, does not display this numerical instability. The distribution functions produced by it are physically reasonable (see Fig. 16). This better stability makes the SW Hermite method a better candidate for long time-simulations.

While the SW Hermite methods (even and odd order) were more stable and performed more accurately than the AW Hermite method, these two SW Hermite methods yielded very similar results. For the simulations shown here, the maximum momentum conservation errors (during the linear growth or damping phase) were 1.3×10^{-3}% (even-order SW) and 2.2×10^{-7}% (odd-order SW). Similarly, energy conservation errors were 2.4×10^{-5}% (even) and 2.3×10^{-4}% (odd). Errors in the conservation of the integral of f^2 were less than 1.8×10^{-4}% for both methods. As we see in Table 8, modeling of linear phenomena was not noticeably affected by these small errors in conservation. Table 4 shows the maximum errors in four conserved quantities over the entire run from initial time to saturation of the BOT instability.

DISCUSSION

The methods described in this article have been designed for modeling plasmas and beams with significant velocity spread relative to their drift velocity. Cold charged-particle beams with widely different drift velocities would be difficult to model efficiently using these Hermite based schemes because spectral methods, in general, use an effective phase-space grid with limited velocity resolution. Simulations of systems with large regions of empty phase-space would require prohibitively large Fourier and Hermite expansion orders in order to obtain moderate accuracy.

The Hermite-based methods that we have described are well suited to high accuracy simulations of warm plasmas, especially when there are subtle or small scale features such as "cat's eyes." We have seen that for such plasmas, the Hermite-based method, with proper velocity scaling, can be far more accurate and efficient than PIC methods. And while PIC methods are computationally simple, the enormous number of particles required to match the accuracy of spectral methods clearly makes Hermite methods an attractive option.

Of the two Hermite methods described, symmetrically weighted (SW) and the previously studied asymmetrically weighted (AW), we have seen that the SW Hermite method is the more accurate and robust. The numerical instability that lurks inside the AW Hermite functional weighting (due to the nonconservation of J) makes it a questionable choice for long-time plasma simulations. By contast, the SW Hermite method, with proper scaling, appears well suited to high accuracy long term simulations.

While we have not extensively reported any long-time simulations here, we have investigated their requirements. The use of velocity scaling has greatly improved the previously reported performance of the Hermite methods [21]. Because the plasma is collisionless there will be growth of small scales (filamentation [13]) and the truncation error will become increasingly problematic. We will investigate the use of Klimas filtering [11, 13] to avoid filamentation in the symmetric Hermite method in another paper.

While Hermite based spectral methods for plasma kinetics simulation have been tried and largely abandoned before [14, 18, 19, 21], the two new ideas explored in this paper—velocity scaling and the use of a symmetric weighting—give new life to this approach.

APPENDIX A: EVALUATION OF SPLITTING ACCURACY

To evaluate the accuracy of the splitting scheme in Eq. (5), we begin by first writing the Vlasov equation in terms of the integro-differential operators Ω_x and $\Omega_u(t)$ acting on the distribution $\mathbf{f}(t) = f(x, u, t)$

$$\frac{\partial \mathbf{f}(t)}{\partial t} = [\Omega_x + \Omega_u(t)]\mathbf{f}(t), \tag{A.1}$$

where $\Omega_x = -u\partial/\partial x$ and $\Omega_u(t) = -E(x, t)\partial/\partial u$. The time-dependence of the E-field is stated implicitly in the integral operator Ω_u. Taylor expanding Eq. (A.1), we may advance the initial system state $\mathbf{f}(t_o)$ forward in time one time-step Δt using

$$\mathbf{f}_{exact}(t_o + \Delta t) = \mathbf{f}(0) + \Delta t\, \dot{\mathbf{f}}(t)|_{t=t_o} + \frac{\Delta t^2}{2}\ddot{\mathbf{f}}(t)\bigg|_{t=t_o} + O(\Delta t^3) \tag{A.2}$$

$$= \left[I + (\Omega_x + \Omega_{uo})\Delta t + \left((\Omega_x + \Omega_{uo})^2 + \dot{\Omega}_{uo}\right)\frac{\Delta t^2}{2} + O(\Delta t^3)\right]\mathbf{f}(t_o), \tag{A.3}$$

where the operators Ω_{uo} and $\dot{\Omega}_{uo} = -\dot{E}(x, t_o)\partial_u$ use E-field information from the system state $\mathbf{f}(t_o)$ at time t_o.

Similarly, we may write the solutions of the X-shift and V-shift,

$$\mathbf{X}_{\Delta t/2} \equiv \mathbf{f}(t_a) = \left(I + \frac{\Delta t}{2}\Omega_x + \frac{\Delta t^2}{8}\Omega_x^2 + \cdots\right)\mathbf{f}(t_o) \tag{A.4}$$

$$\mathbf{V}_{\Delta t} \equiv \mathbf{f}(t_b) = \left(I + \Delta t\Omega_u(t_a) + \frac{\Delta t^2}{2}\left(\dot{\Omega}_u(t_a) + \Omega_u^2(t_a)\right) + \cdots\right)\mathbf{f}(t_a) \tag{A.5}$$

and multiply these expansions as shown in Eq. (5) to find that

$$\mathbf{f}_{split}(\Delta t) = \left[I + (\Omega_x + \Omega_{ua})\Delta t + \left[\dot{\Omega}_{ua} + (\Omega_x + \Omega_{ua})^2\right]\frac{\Delta t^2}{2}\right]\mathbf{f}(t_o) + O(\Delta t^3), \tag{A.6}$$

where Ω_{ua} and $\dot{\Omega}_{ua}$ use the field and current information from the system state *after* the first advection at "time" t_a.

Subtracting Eqs. (A.3) and (A.6), we see the difference is

$$\mathbf{f}_{exact}(\Delta t) - \mathbf{f}_{split}(\Delta t) = \Delta t(\Omega_{uo} - \Omega_{ua}) + \frac{\Delta t^2}{2}\left[(\dot{\Omega}_{uo} - \dot{\Omega}_{ua}) + (\Omega_{uo} + \Omega_x)^2 - (\Omega_{ua} + \Omega_x)^2)\right] + O(\Delta t^3). \tag{A.7}$$

In the splitting method suggested by Cheng and Knorr [9], the E-field is calculated at "time" t_a and held *constant* during the acceleration phase. Then because $E(x, t_a) = E(x, 0) + (\Delta t/2)\dot{E}(x, 0) + O(\Delta t^2)$, the acceleration operators Ω_{ua} and $\dot{\Omega}_{ua}$ satisfy

$$\Omega_{ua} = \Omega_{uo} + \frac{\Delta t}{2}\dot{\Omega}_{uo} + O(\Delta t^2) \tag{A.8}$$

$$\dot{\Omega}_{ua} = 0. \tag{A.9}$$

The first-order error in Eq. (A.8) from calculating the E-field at "time" t_a cancels the second-order error that arises from holding the E_a constant in Eq. (A.7). Therefore, overall, the error in Cheng and Knorr's splitting method can be written

$$\mathbf{f}_{exact}(\Delta t) - \mathbf{f}_{split}(\Delta t) = O(\Delta t^3). \tag{A.10}$$

This is the splitting method we shall use in the simulations included in this article. It is not known to this author (JWS) whether or not an accuracy evaluation for the split Vlasov system has been previously performed.

ACKNOWLEDGMENTS

This research was supported by a National Science Foundation Grant ECS-9358344. One of the authors (JWS) was partially supported by the Department of Energy Magnetic Fusion Science Fellowship under the auspices of the Oak Ridge Institute for Science and Engineering.

REFERENCES

1. L. Landau, On the vibrations of the electronic plasma, *J. Phys. USSR* **10**(1) (1946).
2. J. D. Jackson, Longitudinal plasma oscillations, *J. Nucl. Energy Part C: Plasma Phys.* **1**, 171 (1960).
3. A. J. Klimas and J. Cooper, Vlasov-Maxwell and Vlasov-Poisson equations as models of a one-dimensional electron plasma, *Phys. Fluids*, **26**(2), February 1983.
4. C. K. Birdsall and A. B. Langdon, *Plasma Physics Via Computer Simulation* (IOP, Philadelphia, 1991).
5. L. Demeio and J. P. Holloway, Numerical simulations of BGK modes, *J. Plasma Phys.* **46**, 63 (1991).
6. J. A. Byers and J. Killeen, Finite-difference methods for collisionless plasma models, in *Methods In Computational Physics*, Vol. 9 (Plasma Physics) (Academic Press, New York, 1970), p. 259.
7. L. R. T. Gardner and G. A. Gardner, A locally one-dimensional space time finite element method, in *Numerical Methods for Non-linear Problems, Proceedings of the International Conference, Dubrovnik, Yugoslavia, 1986*, p. 813.
8. H. L. Berk and K. V. Roberts, *The water-bag model*, in *Methods In Computational Physics*, Vol. 9 (Plasma Physics) (Academic Press, 1970), p. 88.
9. C. Z. Cheng and G. Knorr, The integration of the Vlasov equation in configuration space, *J. Comput. Phys.* **22**, 330 (1976).
10. D. Nunn, A novel technique for the numerical simulation of hot collision-free plasma; Vlasov hybrid simulation, *J. Comput. Phys.* **108**(1), 180 (1993).
11. A. J. Klimas, A method for overcoming velocity space filamentation problem in collisionless plasma model solutions, *J. Comput. Phys.* **68**(1), 202 (1987).
12. C. Canuto, M. Y. Hussaini, A. Quarteroni, and T. A. Zang, *Spectral Methods in Fluid Dynamics* (Springer-Verlag, Berlin, 1988).
13. A. J. Klimas and W. M. Farrell, A splitting algorithm for Vlasov simulation with filamentation filtration, *J. Comput. Phys.* **110**(1), 150 (1994).

14. F. C. Grant and M. R. Feix, Fourier-Hermite solutions of the Vlasov equation in the linearized limit, *Phys. Fluids* **10**(4), 696 (1967).
15. A. Ghizzo, B. Izrar, P. Bertrand, E. Fijalkow, M. R. Feix, and M. Shoucri, Stability of Bernstein-Greene-Kruskal plasma equilibria. Numerical experiments over a long time, *Phys. Fluids* **31**(1), 72 (1988).
16. M. Shoucri and G. Knorr, Numerical integration of the Vlasov equation, *J. comput. Phys.* **14**, 84 (1974).
17. M. Abramowitz and I. A. Stegun, *Handbook of Mathematical Functions* (Dover, New York, 1972).
18. T. P. Armstrong, Numerical studies of the nonlinear Vlasov equation, *Phys. Fluids* **10**, 1269 (1967).
19. T. Armstrong and D. Montgomery, Asymptotic state of the two-stream instability, *Plasma of Phys.* **1**(4), 425 (1967).
20. M. Shoucri and R. R. J. Gagne, Numerical solution of a two-dimensional Vlasov equation, *J. Comput. Phys.* **25**(2), 94 (1977).
21. R. R. J. Gagne and M. M. Shoucri, A splitting scheme for the numerical solution of a one-dimensional Vlasov equation, *J. Comput. Phys.* **24**, 445 (1977).
22. J. P. Boyd, Asymptotic coefficients of Hermite function series, *J. Comput. Phys.* **54**, 382 (1984).
23. T. Tang, The Hermite spectral method for Gaussian-type functions, *SIAM J. Sci. Comput.* **14**, 594 (1993).
24. J. P. Holloway, Spectral velocity discretizations for the Vlasov-Maxwell equations, *Trans. Theory and Statistical Phys.* **25**, 1 (1996).
25. R. C. Harding, Response of a one-dimensional Vlasov plasma to external electric fields, *Phys. Fluids* **11**, 2233 (1968).
26. G. Joyce, G. Knorr, and H. K. Meier, Numerical integration methods of the Vlasov equation, *J. Comput. Phys.* **8**, 53 (1971).
27. G. Knorr and M. Shoucri, Plasma simulation as eigenvalue problem, *J. Comput. Phys.* **14**, 1 (1974).
28. W. H. Press, B. P. Flannery, S. A. Teukolsky, and W. T. Vetterling, *Numerical Recipes: The Art of Scientific Computing (FORTRAN)* (Cambridge Press University, 1989).
29. J. W. Schumer, *Optimized 1d-1v Vlasov-Poisson Simulations Using Fourier–Hermite Spectral Discretizations*, dissertation (University of Michigan, February 1997).
30. D. R. Durran, The third-order Adams-Bashforth method: An attractive alternative to leapfrog time differencing, *Monthly Weather Review* **119**, 702 (1991).
31. P. J. Morrison, The Maxwell-Vlasov equations as a continuous Hamiltonian system, *Phys. Letters* **80**A, 383 (1980).
32. J. P. Holloway, On numerical methods for Hamiltonian PDEs and a collocation method for the Vlasov-Maxwell equations, *J. Comput. Phys.* **129**, 121 (1996).
33. N. G. Van Kampen, On the theory of stationary waves in plasmas, *Physica* **21**, 949 (1955).